The Astrophysical Journal, 952:86 (17pp), 2023 July 20 https://doi.org/10.3847/1538-4357/acd5d5

SN2019wxt: An Ultrastripped Supernova Candidate Discovered in the Electromagnetic Follow-up of a Gravitational Wave Trigger

Hinna Shivkumar[1], Amruta D. Jaodand[2], Arvind Balasubramanian[3], Christoffer Fremling[2], Alessandra Corsi[3], Anastasios Tzanidakis[4], Samaya Nissanke[5,6], Mansi Kasliwal[2], Murray Brightman[2], Geert Raaijmakers[5], Kristin Kruse Madsen[7], Fiona Harrison[2], Dario Carbone[8], Nayana A. J.[9], Jean-Michel Désert[1], and Igor Andreoni[10,11,12]

[1] Anton Pannekoek Institute for Astronomy, University of Amsterdam, Science Park 904, 1098 XH Amsterdam, The Netherlands; h.shivkumar@uva.nl
[2] California Institute of Technology, 1200 E. California Boulevard, Pasadena, CA 91125, USA; ajaodand@caltech.edu
[3] Department of Physics and Astronomy, Texas Tech University, Box 1051, Lubbock, TX 79409-1051, USA
[4] University of Washington, 3910 15th Avenue NE, Seattle, WA 98195, USA
[5] GRAPPA, Anton Pannekoek Institute for Astronomy and Institute of High-Energy Physics, University of Amsterdam, Science Park 904,1098 XH Amsterdam, The Netherlands
[6] Nikhef, Science Park 105, 1098 XG Amsterdam, The Netherlands
[7] CRESST and X-ray Astrophysics Laboratory, NASA Goddard Space Flight Center, Greenbelt, MD 20771, USA
[8] University of the Virgin Islands, 2 Brewers Bay Road, Charlotte Amalie, USVI 00802, USA
[9] Indian Institute of Astrophysics, II Block, Koramangala, Bangalore 560034, India
[10] Joint Space-Science Institute, University of Maryland, College Park, MD 20742, USA
[11] Department of Astronomy, University of Maryland, College Park, MD 20742, USA
[12] Astrophysics Science Division, NASA Goddard Space Flight Center, Mail Code 661, Greenbelt, MD 20771, USA
Received 2022 August 19; revised 2023 March 29; accepted 2023 April 12; published 2023 July 19

Abstract

We present optical, radio, and X-ray observations of a rapidly evolving transient SN2019wxt (PS19hgw), discovered during the search for an electromagnetic counterpart to the gravitational-wave (GW) trigger S191213g. Although S191213g was not confirmed as a significant GW event in the off-line analysis of LIGO-Virgo data, SN2019wxt remained an interesting transient due to its peculiar nature. The optical/near-infrared (NIR) light curve of SN2019wxt displayed a double-peaked structure evolving rapidly in a manner analogous to currently known ultrastripped supernovae (USSNe) candidates. This double-peaked structure suggests the presence of an extended envelope around the progenitor, best modeled with two components: (i) early-time shock-cooling emission and (ii) late-time radioactive ^{56}Ni decay. We constrain the ejecta mass of SN2019wxt at $M_{\rm ej} \approx 0.20 M_{\odot}$, which indicates a significantly stripped progenitor that was possibly in a binary system. We also followed up SN2019wxt with long-term Chandra and Jansky Very Large Array observations spanning ∼260 days. We detected no definitive counterparts at the location of SN2019wxt in these long-term X-ray and radio observational campaigns. We establish the X-ray upper limit at 9.93×10^{-17} erg cm^{-2} s^{-1} and detect an excess radio emission from the region of SN2019wxt. However, there is little evidence for SN1993J- or GW170817-like variability of the radio flux over the course of our observations. A substantial host-galaxy contribution to the measured radio flux is likely. The discovery and early-time peak capture of SN2019wxt in optical/NIR observations during EMGW follow-up observations highlight the need for dedicated early, multiband photometric observations to identify USSNe.

Unified Astronomy Thesaurus concepts: Core-collapse supernovae (304); Supernovae (1668); Ejecta (453); Stellar remnants (1627); Gravitational wave sources (677); X-ray sources (1822); X-ray astronomy (1810); Radio interferometry (1346); Extragalactic radio sources (508); Spectral line identification (2073); Transient detection (1957); Transient sources (1851)

Supporting material: data behind figure

1. Introduction

Massive stars at the endpoints of their lives undergo mass loss through the ejection of some or all of their hydrogen (and possibly helium) envelopes, eventually collapsing in what are known as stripped-envelope core-collapse supernovae (SESNe; Clocchiatti et al. 1996; Filippenko 1997; Gal-Yam et al. 2014). The extent to which the outer layers of massive stars are stripped dictates their spectroscopic classification into their various subclasses. Partial stripping in Type IIb supernovae (SNe) is supported by the presence of Balmer lines, while strong stripping in Type Ic SNe is evident by the absence of both hydrogen and helium lines. The current population of SESNe suggests that the ejection of the progenitor envelopes can be driven by (a) mass loss via stellar wind (Begelman & Sarazin 1986; Woosley & Weaver 1995; Pod 2001), or (b) mass transfer during binary interaction (Podsiadlowski et al. 1992; Yoon et al. 2010; Smith et al. 2011; Yoon 2017).

Large uncertainties currently persist in our understanding of the progenitors of SESNe. Specifically, if any links exist between the various SESNe subclasses, and if different subclasses have preferred mass-loss mechanisms. At the same time, the observational picture of SESNe has been evolving in the last few years as wide-field optical surveys have accelerated

the rate of discovery and started filling up the luminosity "gap" between novae and SNe in the luminosity-duration phase space (Nugent et al. 2015). In particular, optimized follow-up observations have opened up the parameter space for the characterization of rapidly evolving, low-luminosity ($L_{\rm bol} = 10^{42}$ erg s^{-1}) transients—resulting in a growing population of ultrastripped SNe (USSNe; Kasliwal et al. 2010; Drout et al. 2013; De et al. 2018a, 2018b; Jacobson-Galán et al. 2020).

The progenitors of USSNe undergo extreme envelope stripping via two stages of common envelope evolution, with a first phase of mass transfer through Roche-lobe overflow, leading to a He-star neutron star (NS) system. The second mass-transfer phase in the resulting He-star NS system involves the stripping of the He-star leading to a stripped He-star NS system with a He-rich envelope. The core collapse of the stripped He star triggers a maximally stripped supernova (SN) explosion known as a USSN. This explosion is accompanied by the ejection of $\approx 0.01 M_{\odot}$ of the star mass. Such USSNe are then expected to evolve into binary neutron star (BNS) systems (Tauris et al. 2013, 2015, 2017). In fact, light curves of these SNe display double peaks in both bluer and redder bands, indicating the presence of an extended envelope around the progenitor (Nakar & Piro 2014). The combination of shock-cooling emission (SCE) and the radioactive decay of ^{56}Ni has been used to explain this double-peaked structure and rapid evolution in the light curves of currently known USSNe candidates such as SN2019dge (Yao et al. 2020) and iPTF14gqr (De et al. 2018b).

In this work, we present multiwavelength observations spanning optical, radio, and X-ray wave bands for one such puzzling USSN candidate dubbed SN2019wxt. SN2019wxt was discovered by the PanSTARRS Search for Kilonovae survey (as PS19hgw) during their electromagentic (EM) follow-up of LIGO-Virgo GW trigger, S191213g (flagged as a BNS merger event; LIGO Scientific Collaboration, & Virgo Collaboration 2019a). A follow-up observational campaign across the EM spectrum was encouraged because SN2019wxt was located in the 80% confidence contour of the S191213g's skymap (LIGO Scientific Collaboration & Virgo Collaboration 2019b) with its distance being consistent with the estimated luminosity-distance range for S191213g (McBrien et al. 2019a). Moreover, the optical light curve of SN2019wxt displayed a very fast decline in comparison to previously known, rapidly evolving, hydrogen-free supernovae such as SN2008ha or SN2010ae (Valenti et al. 2009; Foley et al. 2009; Stritzinger et al. 2014). Although in the off-line analysis of GW data S191213g was demoted as a significant GW candidate (The LIGO Scientific Collaboration et al. 2021), SN2019wxt remains a very interesting transient. Our multiband optical observations show a double-peaked, rapidly declining light curve resembling that of the USSNe candidates iPTF14gqr (De et al. 2018b) and SN2019dge (Yao et al. 2020).

We outline the interesting nature of SN2019wxt based on a campaign of high-cadence optical observations and other complementary data from radio and X-ray observational campaigns. Our work is organized as follows. Section 2 outlines the observational properties of SN2019wxt and its multiband follow-up observations. Section 3 outlines the data analysis techniques used for optical, X-ray, and radio observations. Here we also present a fully Markov Chain Monte Carlo (MCMC) parameter estimation for the characterization of SN2019wxt's physical properties. Finally, in Section 4, we provide an interpretation of the results obtained from this comprehensive data set and their implications in the broader context of stellar evolution.

2. Discovery and Panchromatic Follow-up

2.1. SN2019wxt (PS19hgw)

SN2019wxt was discovered on 2019 December 16 UTC 07:19:12 (MJD 58833.305) as a source at an optical magnitude of 19.38 ± 0.05 in the PS1 i band (McLaughlin et al. 2019; McBrien et al. 2019a). It was localized to R.A. = 01:55:41.941, decl. = +31:25:04.55, and found to be associated with the compact host galaxy KUG 0152+311.[13] The association of SN2019wxt with KUG 0152+311 was confirmed by early optical spectra (Dutta et al. 2019), which displayed standard galaxy lines at a redshift of $z = 0.036$ (luminosity distance, $d = 144$ Mpc from the NASA/IPAC Extragalactic Database (NED), assuming $H_0 = 73$ km s^{-1} Mpc^{-1}, $\Omega_m = 0.27$, and $\Omega_{\rm vacuum} = 0.73$). This distance estimate from optical observations placed SN2019wxt within an 80% confidence interval of the LIGO-VIRGO localization skymap (at a luminosity-distance range of S191213g $d_L = 201 \pm 81$ Mpc; McBrien et al. 2019a; LIGO Scientific Collaboration & Virgo Collaboration 2019b). The offset between SN2019wxt and the host galaxy was observed to be 0.″5S, 7.″7 E, with a projected distance of 6.7 kpc from the galactic center (McLaughlin et al. 2019).

The presence of helium in optical spectra (Vogl et al. 2019) and rapid photometric evolution further confirmed SN2019wxt as an interesting EM candidate counterpart of S191213g. The rapid decline in brightness was observed to be faster than that for known hydrogen-free SNe (e.g., SN2008ha and SN2010ae; Foley et al. 2009; Valenti et al. 2009; Stritzinger et al. 2014) but slower than the kilonova AT2017gfo associated with GW170817 (e.g., Arcavi et al. 2017a; Cowperthwaite et al. 2017) and the possible white dwarf–NS merger SN2018kzr (Huber et al. 2019; McBrien et al. 2019b). Hence, we triggered a comprehensive, multiband EM follow-up campaign with a host of space- and ground-based telescopes. This observational campaign spanned optical/near-infrared (NIR), X-ray, and radio wave bands. Observations for each of these wave bands are summarized in Tables 7, 8, 9, and 10, respectively.

2.2. Optical/NIR Observations

2.2.1. Photometric Observations

After the initial discovery of SN2019wxt was reported by PanSTARRS (McBrien et al. 2019a; McLaughlin et al. 2019), the Global Relay of Observatories Watching Transients Happen (GROWTH) collaboration conducted further follow-up observations using the Spectral Energy Distribution Machine (SEDM; Blagorodnova et al. 2018) on the Palomar 60 inch telescope (P60; Cenko et al. 2006). The SEDM obtained 180 s exposure-time images of SN2019wxt with the rainbow camera imager for each of the *ugri* filters. These images were processed using a standard Python-based and fully automated reduction pipeline, FPipe (Fremling et al. 2016), which performs host-galaxy subtraction and PSF fitting photometry. Host-galaxy subtraction was performed using

[13] Galaxy morphology and classification from NASA/IPAC Extragalactic Database (NED) http://ned.ipac.caltech.edu. Please also refer to Gaia Collaboration (2020).

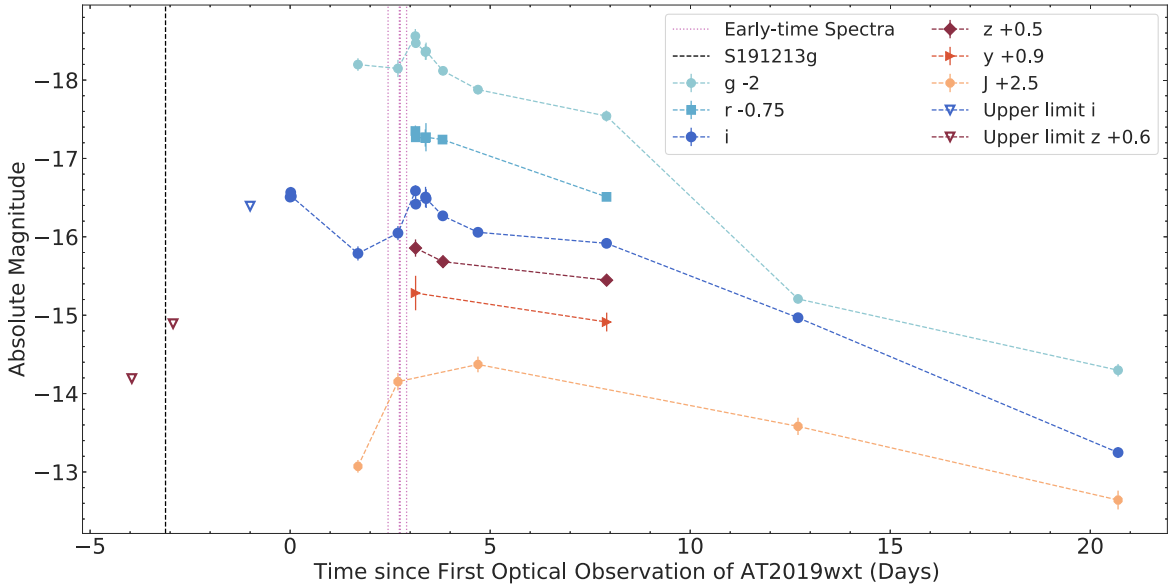

Figure 1. Galactic extinction-corrected optical and NIR light curves of the transient SN2019wxt using the data from Table 7. The cyan, light blue, blue, magenta, dark red, orange, and yellow markers represent photometric data in the *g*, *r*, *i*, *z*, y, and *J* band, respectively, and the markers for each band are connected by a dashed line to visually track the photometric evolution. The magnitudes are offset vertically for better visibility and the times displayed are relative to the first optical observation at MJD 58833.305, used as a reference epoch henceforth. The vertical black dashed line indicates the time of the GW trigger S191213g, for reference. Vertical, dotted, magenta lines indicate epochs where early-time spectroscopic observations were used in this work (see 2.2.2).

Sloan Digital Sky Survey (SDSS) images of KUG 0152+311, and the source photometry was derived in the AB magnitude system (Fremling 2019).

The GROWTH collaboration also obtained 300 s exposure images in *g*, *r*, and *i* filters with the Lulin 1 m Telescope (LOT) located in Taiwan. The LOT magnitudes, also in the AB magnitude system, are calibrated against the PS1 catalog (Kong 2019). Follow-up observations of SN2019wxt were also conducted with the Large Monolithic Imager (Bida et al. 2014) on the 4.3 m Lowell's Discovery Channel Telescope (DCT; located in Arizona) for each of the *griz* filters. The magnitudes are calibrated with the SDSS catalog and are presented in the AB system (Dichiara & a larger Collaboration 2019). Simultaneously, optical observations of SN2019wxt were also undertaken with the three-channel imager 3KK camera (Lang-Bardl et al. 2016) on the 2 m telescope at the Wendelstein Observatory. Observations were obtained on five epochs for each of the filters (*g'*, *i'*, *J*). Aperture photometry was performed using eight comparison stars within the field of view of the detector. Magnitude errors include statistical errors in the measurement of the magnitude of SN2019wxt and in the zero-point calculation (Hopp et al. 2020).

The observations and photometric measurements are summarized in Table 7 and span ≈20.7 days since the initial detection. The multiband light curves are collectively displayed in Figure 1. We corrected apparent magnitudes for Galactic extinction using the data available on the foreground galactic extinction for the host galaxy KUG 0152+311 on NED for each band. The NED calculates Galactic extinction values assuming the Fitzpatrick (1999) reddening law with $R_V \equiv A(V)/E(B-V) = 3.1$.

2.2.2. Spectroscopic Observations

Early-time spectroscopic observations of SN2019wxt were taken on 2019 December 18 and 19 (see Table 8). The initial spectroscopic observations were unable to firmly classify the transient (Dutta et al. 2019; Izzo et al. 2019; Srivastav & Smartt 2019). SN2019wxt showed narrow lines consistent with the host-galaxy redshift of $z = 0.037$, and a blue, relatively featureless continuum with a broad feature at 5400–6200 Å. Vogl et al. (2019) identified the broad feature as He I lines and suggested that SN2019wxt was either a young Type Ib or perhaps Type IIb supernova given the blue continuum. The similarities of the spectra to SN 2011fu (Kumar et al. 2013) prompted Vallely (2019) to classify SN2019wxt as a Type IIb. This supernova classification was subsequently supported by Valeev & Castro-Rodriguez (2019) and Becerra-Gonzalez & a larger Collaboration (2019).

In this work, we use early-time spectroscopic observations obtained with various telescopes, such as: (i) the 2 m Himalayan Chandra Telescope (HCT) at Indian Astronomical Observatory at Hanle; (ii) the 8.2 m Very Large Telescope (VLT) UT1 at European Southern Observatory (ESO) at Paranal Observatory, Chile; (iii) the 3.58 m New Technology Telescope (NTT) at La Silla Observatory, as part of the extended-Public ESO Spectroscopic Survey for Transient Objects (ePESSTO; PI: Smartt); and (iv) the 8.4 m Large Binocular Telescope (LBT) at LBT Observatory in Arizona, USA. The HCT observations were conducted with the Hanle Faint Object Spectrograph Camera (HFOSC2) instrument (Dutta et al. 2019). HCT/HFOSC2 provides low- to medium-resolution grism spectroscopy with a resolution of 150–4500 based on grism settings. HCT observations in this work used grism 7 to provide a resolution of 1200 for the observations in the wavelength range of 3800–7500 Å. The VLT observations were carried out with the FOcal Reducer/low dispersion Spectrograph 2 (FORS2) instrument on UT1 Cassegrain focus in long-slit mode (slit-width of 1″) to obtain spectroscopic observations of SN2019wxt (Vogl et al. 2019). The long-slit mode provides a resolution of 260–2600. ESO-NTT was used with the ESO Faint Object Spectrograph (EFOSC2) on Nasmyth B focus (Müller Bravo et al. 2019). EFOSC2 provides low-resolution spectroscopy of faint objects. The

LBT was used with the Multi-Object Double Spectrograph, which provides a spectral resolution of 103–104 (Vallely 2019).

2.3. X-Ray Observations

We obtained high-resolution (∼1″) X-ray imaging observations of SN2019wxt with the Chandra X-ray. These observations were performed with back-illuminated Advanced CCD Imaging Spectrometer (ACIS)[14] chip S3 in timing exposure (TE) mode. The ACIS S3 chip provided an energy resolution of 95 eV (at 1.49 keV) at the aim point (in this case, the S3 chip), a timing resolution of 3.2 s, and a field of view of $8\farcm3 \times 8\farcm3$. The TE mode allowed for the Very Faint (VFAINT) telemetry format, which reduced background contamination, especially at lower and higher energy ranges for low count rates and/or extended sources.

Our trigger criterion for these Chandra observations was a well-localized (∼a few arc seconds) BNS merger within 200 Mpc. At the time of initial discovery, SN2019wxt was a primary and interesting candidate counterpart to S191213g given the red evolution and photometric evolution. Moreover, the host-galaxy redshift firmly placed it within 3σ (100 Mpc) of the S191213g candidate (201 ± 81 Mpc; LIGO Scientific Collaboration & Virgo Collaboration 2019b). Extrapolating from GW170817 (Haggard et al. 2017), we expected at least 10 photons in one 100 ks exposure. The observations were scheduled to span a 6 month period post initial GW trigger (a detailed summary of the observations can be found in Table 9). This timescale was motivated by continued X-ray observations of GW170817, 3.5 yr post the BNS merger event (Hajela et al. 2022). Given the lower total mass prediction for S191213g than GW170817, we expected a long-lived supermassive or stable NS remnant with X-ray emission from the magnetar wind nebula emerging at later times, and hence continued the SN2019wxt follow-up.

2.4. Radio Observations

Radio observations of the SN2019wxt field were carried out using the Karl G. Jansky Very Large Array (VLA) between UT 2019 December 19 and 2020 August 20 in the D (VLA:19A-222; PI: Troja), C, and B configurations (VLA:18B-320 and VLA:20A-115; PI: Frail). These observations were performed at nominal central frequencies of 10 GHz (*X* band), 15 GHz (*Ku* band), and 22 GHz (*K* band), and are summarized in Table 10. The raw data were calibrated using the `CASA` (McMullin et al. 2007) automated calibration pipeline, and imaging analysis was performed using the `CASA` task `tclean`. The relative observational epochs in column (2) of Table 10 are with respect to the first optical detection (reference epoch; MJD 58833.305).

In Table 10 we also present flux densities of SN2019wxt and its host galaxy KUG 0152+311 (in units of μJy = 10^{-29} erg s^{-1} cm^{-2} Hz^{-1}). The flux density of SN2019wxt is the maximum value obtained from a circular region of one nominal synthesized beamwidth[15] centered on SN2019wxt using the `CASA` task `imstat`. Using this same task in the residual image, we computed rms flux density within a 30″ circular region centered on SN2019wxt. The flux calibrator, 3C48, used in these computations has been undergoing a flare since 2018 January.[16] Hence, we added additional 10% (*X* and *Ku* band) and 20% (*K* band) absolute flux calibration errors in quadrature to the above rms values. These final flux density errors are presented in Table 10. Any observations with a resulting flux density lower than 3 × the final flux density error were designated as upper limits. All *K* band observations are therefore upper limits.

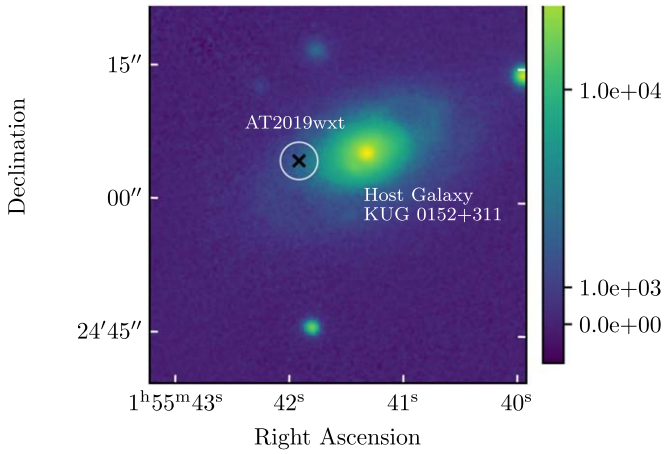

Figure 2. Pan-STARRS *i*-band image overplotted with the position of SN2019wxt (cross marks the optical position) and a circle of radius 2.″1 along with the extent of the host galaxy KUG 0152+311.

We then obtained the peak flux density of the host galaxy KUG 0152+311 from `CASA` task `imstat` in circular regions of radii 2.″1 (*X* band), 1.″4 (*Ku* band), and 3.″1 (*K* band), centered at $01^{h}55^{m}41\overset{s}{.}363$, $31^{h}25^{m}05\overset{s}{.}06$ in all configurations (so as to account for extended emission from the host, see Figure 2). Absolute flux calibration errors as described above were added in quadrature to the rms value obtained from the large 30″ region around SN2019wxt to obtain the error on the galaxy's peak flux density.

3. Data Analysis and Results

3.1. Optical/NIR Data Analysis

3.1.1. Light curve Evolution

The earliest optical detection of SN2019wxt was obtained in the *i* band and the light curve in this band displayed a prominent double-peaked structure (evident from Figure 1). While the *g* band confirms a similar double-peaked structure, we only observe the tail end of the first peak due to a lack of early-time observations. We lack early-time observations during the rise to the second peak in the *r*, *z*, and *y* bands, so in these bands, we can only report a decline in brightness relative to the time of the second peak in *g* and *i* bands. We assume an explosion time of $t_{exp} \approx -4$ days, which is based on the earliest upper limits available from *z*-band observations of SN2019wxt.

The rate of evolution of the optical light curve is quite rapid and comparable to the previously known fastest, extragalactic transients (further discussed in Section 4). For example, in the *i* band, the first peak ($M_{i,peak1} \approx -16.5 \pm 0.05$ mag) displays a rapid decline in brightness, reaching a minimum within ≈1.7

[14] For more details please refer to Chapter 6 of https://cxc.harvard.edu/proposer/POG/pdf/MPOG.pdf, Proposers' Observatory Guide, Cycle 24.
[15] https://science.nrao.edu/facilities/vla/docs/manuals/oss/performance/resolution
[16] https://science.nrao.edu/facilities/vla/docs/manuals/oss/performance/fdscale

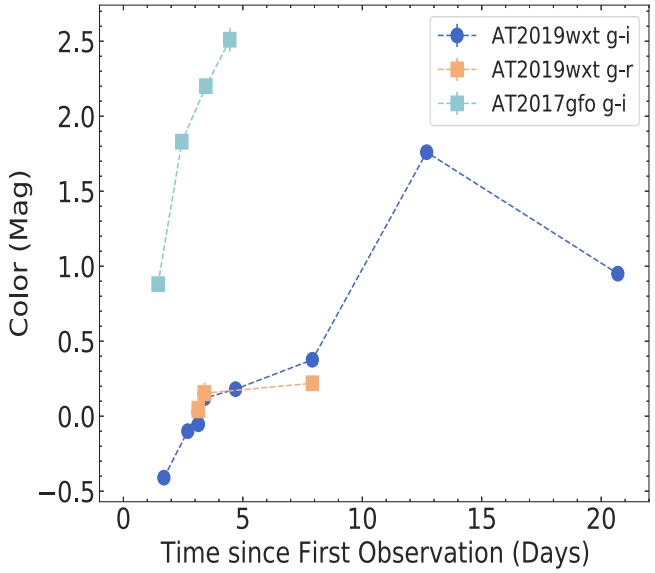

Figure 3. Color evolution of SN2019wxt compared to that of the GW170817 postmerger kilonova, AT2017gfo. Blue solid circles show the $g-i$ color evolution for SN2019wxt and orange filled squares show the $g-r$ color evolution for SN2019wxt. A red evolution through the $g-i$ color evolution is observed followed by a peak at ∼13 days post initial transient detection. Meanwhile, cyan filled squares and dashed connector lines between them show the $g-i$ color evolution for AT2017gfo.

days. A subsequent rebrightening is then observed, which leads to a second peak ($M_{\mathrm{i,peak2}} \approx -16.6 \pm 0.07$ mag) at ≈3.1 days since initial detection. After the second peak, the light curves exhibit a rapid decline in the bluest bands (g and i), whereas a relatively shallow (≈0.108 mag day^{-1}) decline is seen in the redder NIR J band. Although, we note that this shallow decline may just be a result of a lack of observations in the J band. Interestingly, a nonuniform behavior in the light curve evolution is observed post the second peak. It can be characterized by an initial rapid decline up to ≈5 days at an average rate of ≈0.43 mag day^{-1} in the g band and ≈0.27 mag day^{-1} in the i band. Following this phase, we observe a decline in the light curve that is relatively slower and accompanied by a shoulder at ≈8 days. This long-term evolution of the light curve is visible in the g, i, and J bands. Similar behavior with distinct evolution rates between redder and bluer bands has been observed in general in SNe as well as the kilonova AT2017gfo (Cowperthwaite et al. 2017).

To understand the color evolution of SN2019wxt we calculated $g-i$ and $g-r$ colors. To achieve this we initially grouped together observations from different bands performed either simultaneously or on the same day. The color evolution obtained as such is displayed in Figure 3 and shows $g-i$ color red evolution from 1.7 days to about 6 days at a rate of ≈0.13 mag day^{-1}. This color evolution is slower than that of the kilonova AT2017gfo. This further confirms the distinct and complex evolutionary behavior across different bands.

3.1.2. Spectral Energy Distribution

We construct the spectral energy distribution (SED) of SN2019wxt using multiband photometric observations spanning *grizyJ* bands.

We first grouped these observations from different bands that were performed either simultaneously or on the same day. Of

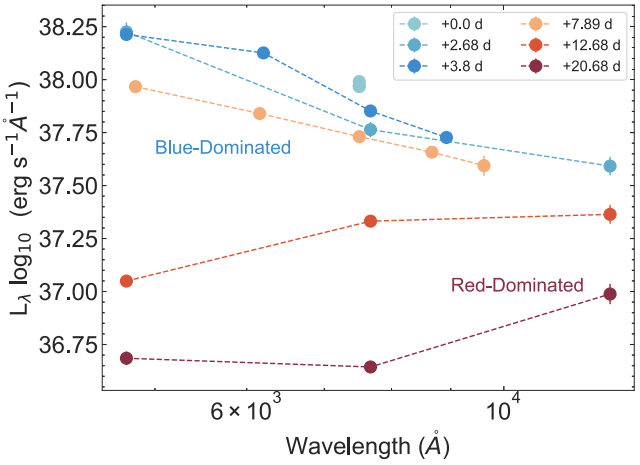

Figure 4. The spectral energy distribution (SED) of SN2019wxt at six representative epochs. The cyan, light blue, blue, yellow, dark red, and magenta circular markers represent six different epochs, respectively, in increasing order, and the markers for each epoch are connected by a dashed line to visually track the evolution of the SED. The early-time emission peaks at bluer wavelengths and we observe a rapid transition to redder wavelengths at late time. All times are relative to the first optical observation as a reference epoch.

the resulting nine epochs, we present six epochs in Figure 4 to compare the temporal evolution of the SED of SN2019wxt.

Initially, emission at bluer wavelengths dominates the SED, and over time, we observe a peak shift to redder wavelengths. Assuming the transient emits as a blackbody, as a first-order approximation we fit a blackbody model to the SED at each epoch using the MCMC implementation via `emcee` package[17] (Foreman-Mackey et al. 2013). This package uses an MCMC ensemble sampler immune to affine transformations (Goodman & Weare 2010). The resulting SED and blackbody fits for each epoch are shown in Figure 5. Our MCMC implementation also yielded the blackbody radius, R_{bb}, and temperature of the blackbody, T_{bb}, at each epoch. The bolometric luminosity, L_{bol}, is then calculated using these parameters (see Table 1) with a simple Stefan–Boltzmann law. We also show the evolution of L_{bol}, T_{bb}, and R_{bb} in Figure 6.

3.1.3. Bolometric Light curve Evolution

The bolometric luminosity of SN2019wxt peaks at ≈1.96×10^{42} erg s^{-1} during the first observation. This is followed by a subsequent decline after which a second, lower luminosity peak is observed (≈1.36×10^{42} erg s^{-1}) at ≈3.1 days. After this, we observe a shallow decline in the bolometric luminosity. It should be noted that the L_{bol} value estimated from the first observation (via blackbody fits) has large uncertainty due to the lack of multiband observations.

The blackbody temperature, T_{bb}, reaches a maximum value of ≈9770 K ≈1.5 days after the first observation and rapidly decreases afterward. At ≈3 days after the first observation, T_{bb} approaches a second peak with a maximum of ≈8320 K. On the other hand, the blackbody radius of SN2019wxt increases over time and reaches a maximum (≈$22.76 \times 10^3\ R_{\odot}$) at ≈12.7 days. The inverse trend in T_{bb} and R_{bb} evolution can be explained by an expanding envelope. Moreover, the high initial temperature can be attributed to opaque, ionized material. As the matter expands and cools, the opacity of this material

[17] https://github.com/dfm/emcee

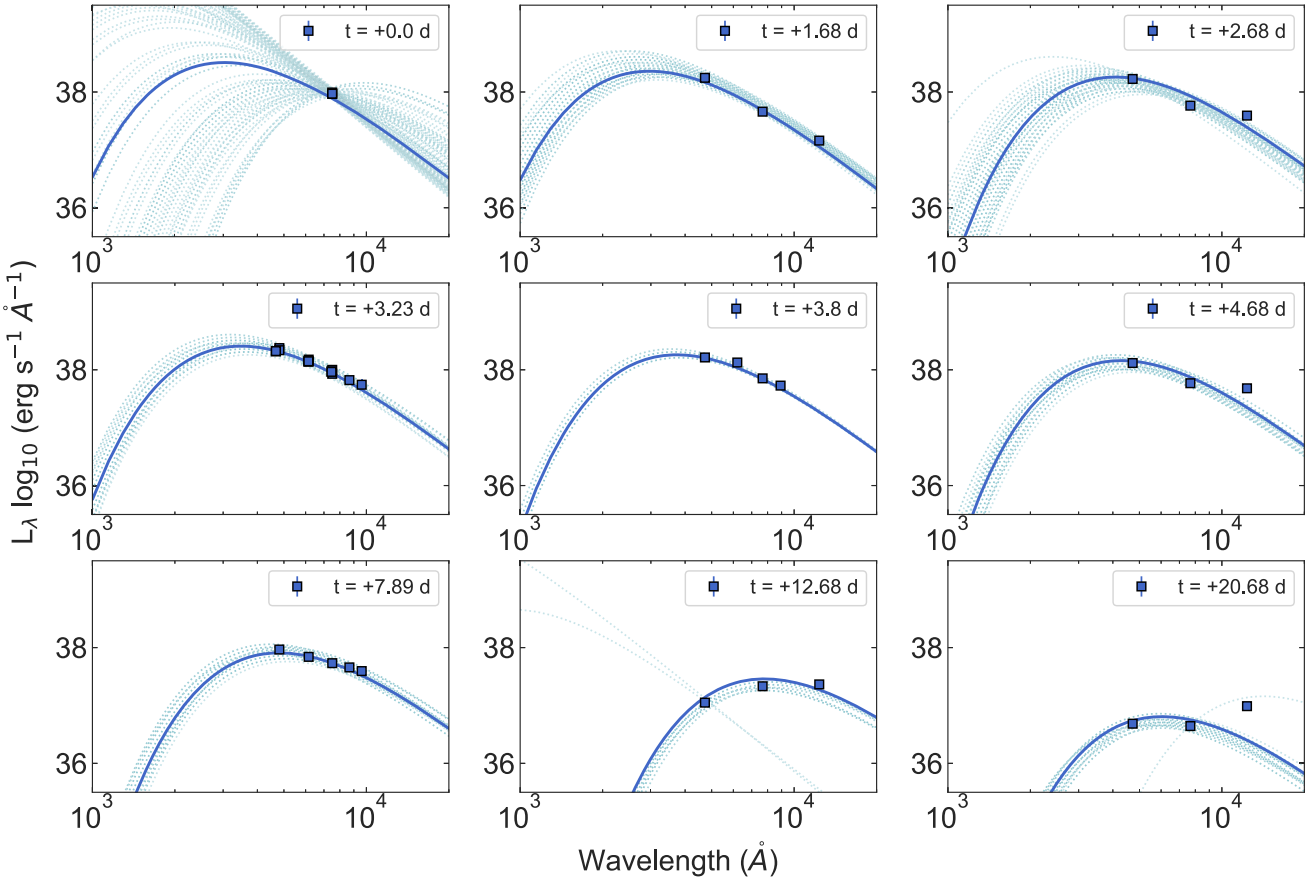

Figure 5. Spectral energy distribution (SED) evolution over eight epochs (days) for SN2019wxt. For each subplot, the square data points indicate the optical photometry at given wavelengths, the solid dark-blue line represents the best-fit blackbody model from the MCMC inference, and the dotted light-blue lines represent the 100 random draws from the MCMC posterior.

should decrease with time due to recombination. Here, it is interesting to note that the red evolution observed in the $g-i$ peaks at ≈12.7 days, which coincides with a maxima in blackbody radius $R_{\rm bb}$ and a minima in blackbody temperature.

We also compare the evolution of the bolometric luminosity, blackbody temperature, and blackbody radius of SN2019wxt to that of: (i) kilonova AT2017gfo; (ii) the USSNe candidates SN2019dge and iPTF14gqr; and (iii) the Ca-rich gap transient iPTF16hgs in Figure 7. As evident from this figure, the light curve of SN2019wxt evolves relatively slower than that of AT2017gfo (Abbott et al. 2017; Andreoni et al. 2017; Arcavi et al. 2017b; Coulter et al. 2017; Cowperthwaite et al. 2017; Drout et al. 2017; Evans et al. 2017; Nicholl et al. 2017; Kasliwal et al. 2017; Lipunov et al. 2017; Pian et al. 2017; Smartt et al. 2017; Tanvir et al. 2017; Troja et al. 2017; Utsumi et al. 2017; Valenti et al. 2017). Following the second peak in the blackbody temperature, $T_{\rm bb}$, of SN2019wxt, the temperature steadily decreases faster than other USSNe candidates but in a manner analogous to iPTF16hgs, a Ca-rich "gap" transient. Moreover, while the photospheric expansion for SN2019wxt is similar to other USSNe, the contraction of the radius evolves on timescales intermediate to the kilonova and Ca-rich gap transients.

3.2. Spectroscopic Analysis

We present early-time spectra for SN2019wxt spanning a net wave band of 3000–10000 Å. These spectra were obtained from 2.45 to 2.75 days post the initial peak and during the flux rise toward the second peak. In all of the spectra, a blue continuum is observed that we fit with a `generic_continuum_fitting` routine available under the Astropy spectroscopy package Specutils.[18] In this analysis, the continuum was modeled by smoothing with a median filter to remove the spikes. The source spectra were then normalized by dividing them with the fitted continuum. To find significant lines in the spectra we used the `find_line_derivative` routine in Specutils, which finds zero crossings in the spectrum derivative and, depending on these, identifies lines above a

Table 1
Evolution of Bolometric Luminosity ($L_{\rm bol}$), Blackbody Radius ($R_{\rm bb}$), and Blackbody Temperature ($T_{\rm bb}$) Obtained from Blackbody Fits to the Spectral Energy Distribution of SN2019wxt at Different Epochs

Epoch (MJD)	$\log_{10}L_{\rm bol}$ (erg s^{-1})	$R_{\rm bb}$ ($10^3R_\odot$)	$T_{\rm bb}$ (10^3K)
58833.3	$42.29^{+2.79}_{-1.47}$	$9.06^{+12.32}_{-19.12}$	$9.12^{+27.95}_{-7.38}$
58835.0	$42.01^{+0.09}_{-0.09}$	$5.72^{+0.54}_{-0.57}$	$9.77^{+0.79}_{-0.73}$
58836.0	$42.05^{+0.13}_{-0.13}$	$11.41^{+1.81}_{-1.79}$	$7.08^{+0.71}_{-0.69}$
58836.4	$42.13^{+0.05}_{-0.05}$	$9.06^{+0.54}_{-0.54}$	$8.32^{+0.32}_{-0.31}$
58837.1	$42.01^{+0.02}_{-0.02}$	$9.06^{+0.19}_{-0.19}$	$7.76^{+0.11}_{-0.11}$
58838.0	$41.97^{+0.07}_{-0.07}$	$11.41^{+1.02}_{-1.04}$	$6.76^{+0.34}_{-0.33}$
58841.2	$41.77^{+0.05}_{-0.05}$	$11.41^{+0.79}_{-0.79}$	$6.03^{+0.23}_{-0.23}$
58846.0	$41.53^{+0.05}_{-0.05}$	$22.76^{+1.59}_{-1.67}$	$3.72^{+0.08}_{-0.08}$
58854.0	$40.77^{+0.08}_{-0.08}$	$5.72^{+0.63}_{-0.64}$	$4.79^{+0.22}_{-0.21}$

[18] https://specutils.readthedocs.io/en/stable/index.html

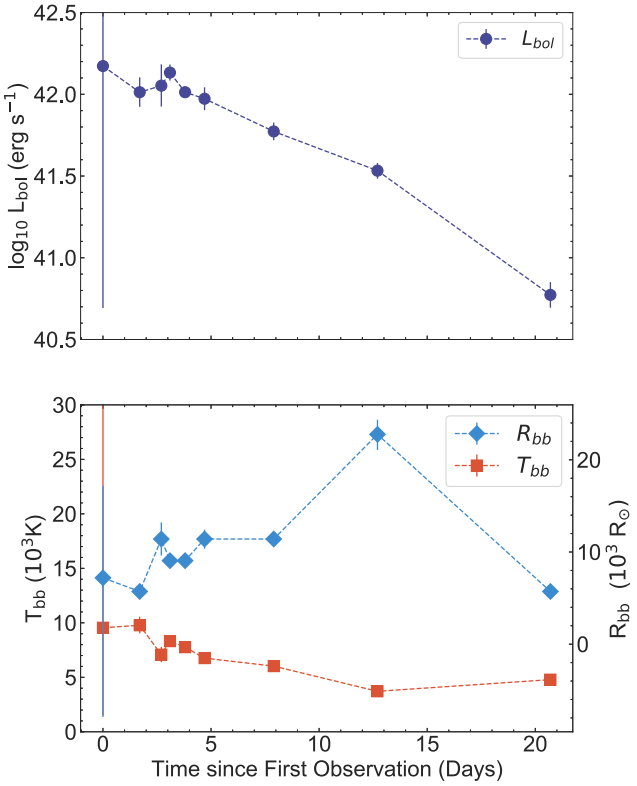

Figure 6. Time evolution of bolometric luminosity, blackbody temperature, and blackbody radius obtained from the blackbody fits on the spectral energy distribution using the multicolor photometry for SN2019wxt using PAN-STARRS, Palomar, Lulin, DCT, and Wendelstein 2 m telescopes. All times are relative to the first optical observation as a reference epoch.

chosen threshold. In our line-finding analysis, we set the threshold at 2σ uncertainty in the flux spectrum for both the emission absorption lines. No absorption lines were found.

Once the central frequencies of possible emission lines were identified, we searched the National Institute of Standards and Technology (NIST) Atomic Spectral Database v5.10[19] to recognize possible atomic spectral lines. The initial line IDs and associated central frequencies obtained from the NIST databases were then crossmatched against spectra of previously identified USSNe candidates, SN2019dge and iPTF14gqr. A summary of significant lines discovered and their presence in spectra from different instruments is presented in Table 2 and Figure 8. The spectral analysis methodology described here is publically available on the GitHub repository[20] along with the optical spectra used in this work.

We observe multiple He I lines (λ5876, λ6678, and λ7065) and one He II λ4686 line. Of the He I lines, we notice a weakening of the He I λ6678 line as the source flux continues to rise; the He II λ4686 line shows a similar attenuation. This line-evolution behavior is even more noticeable in C III (λ5696) and O I λ6300 lines, which vanish over the course of 0.02 days between NTT and VLT-U1 observations. Another C III line at λ4650 is observed along with a weak C IV λ5801 line. Finally, the S II doublet lines—λ6716 and λ6731—appear due to contribution from the host galaxy. A prominent Hα emission line from the galaxy is also observed.

[19] https://www.nist.gov/pml/atomic-spectra-database
[20] https://github.com/amrutajaodand/spectral_fitting

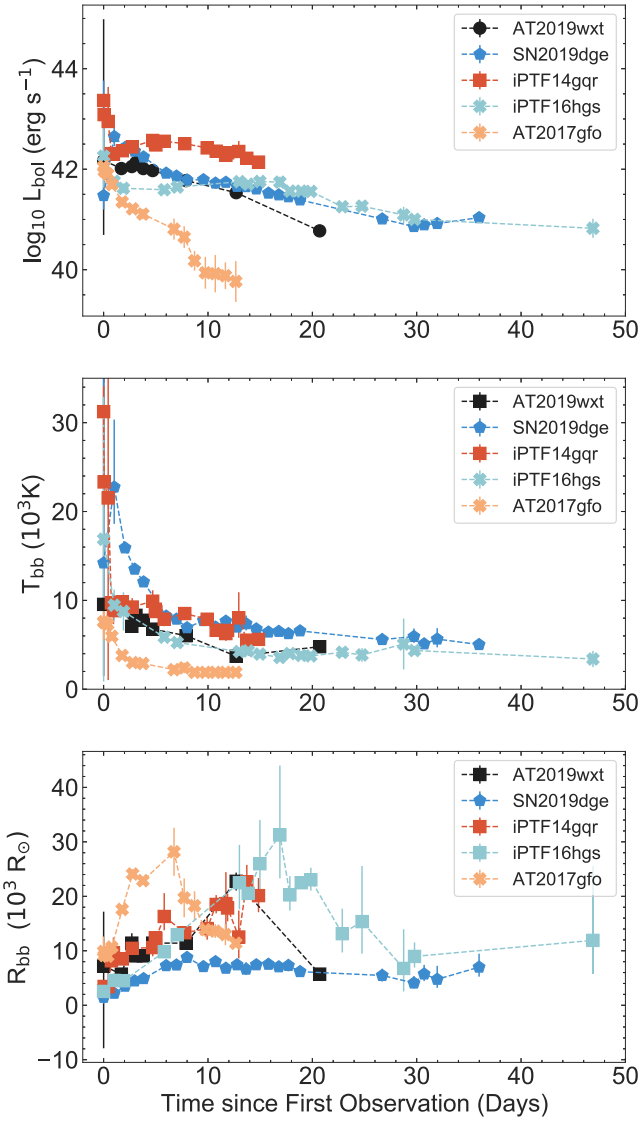

Figure 7. Time evolution of the bolometric luminosity, blackbody temperature, and blackbody radius of SN2019wxt compared with that of the USSNe candidates, SN2019dge and iPTF14gqr; the Ca-rich gap transient, iPTF16hgs; and the kilonova, AT2017gfo. All times are relative to the first optical observation used as a reference epoch for each transient.

3.3. Modeling the Double-peaked Light Curve

Nakar & Piro (2014) show that in the case of progenitors that are not enclosed by an extended envelope, only the blue bands exhibit a double-peaked structure in their light curve due to SCE. In contrast, both the blue and red bands show a double-peaked light curve when an extended, low-mass envelope encloses the compact core. Given the redward nature of the *i* band, we infer that the double-peak structure observed in *i*-band light curves of SN2019wxt (see Figure 1) should indicate a presence of an extended envelope. Moreover, as we showed earlier (Section 1), light curves of core-collapse SNe, which display double peaks in both blue and red bands, have been explained in the past with a combination of two kinds of emission processes—shock-cooling and radioactive decay of ^{56}Ni.

In this section, we follow a similar approach to derive light curve properties from multiband optical and NIR observations of SN2019wxt. We explore a scenario such that the early-time

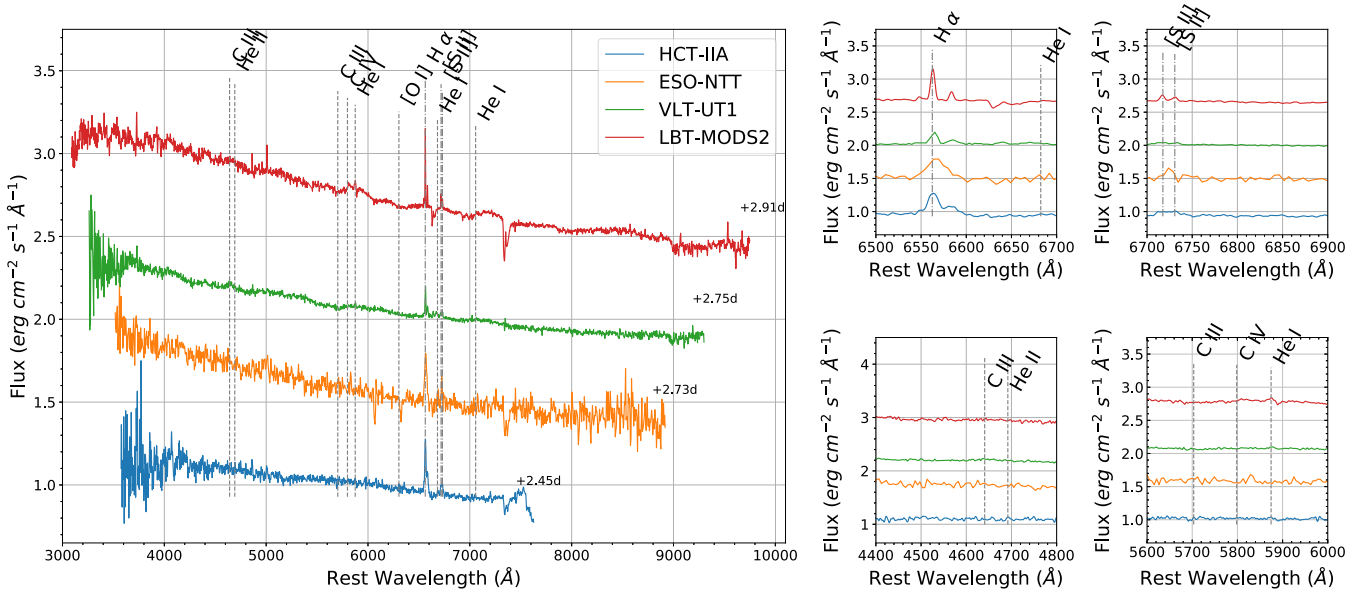

Figure 8. Left: early-time spectra of SN2019wxt arranged in order of their procurement from the bottom to the top of the plot. These spectra were obtained with various telescopes such as HCT-IIA telescope at IAO-Hanle observatory, VLT, and NTT. Each spectrum is normalized and presented with arbitrary offsets for ease of visualization. USSNe and galaxy lines are indicated by vertical dashed and dashed–dotted lines, respectively. Right: subpanels highlight insets around lines detected in the spectra. To note, the central frequency of detected lines may be shifted. The optical spectra are available as Data behind the Figure.

(Data used to create this figure are available.)

Table 2
Summary of Spectral Lines Observed in the Early-time Spectra of SN2019wxt for Various Instruments

Transition	HCT	ePESSTO+	VLT	LBT
He II λ4686	✓	✓	✓	✓
He I λ5876	✓	✓	✓	✓
He I λ6678	✓	✓		
He I λ7065	✓	✓	✓	✓
Hα*	✓	✓	✓	✓
[C III] λ4650	✓	✓	✓	✓
[C III] λ5696	✓	✓		
[C IV] λ5801	✓	✓	✓	✓
[O I] λ6300	✓	✓		
[S II] λ6716*	✓	✓	✓	✓
[S II] λ6731*	✓	✓	✓	✓

Note. The transition lines marked with an asterisk indicate host-galaxy lines.

emission is dominated by SCE from an extended envelope followed by a late-time emission due to radioactive decay of ^{56}Ni. Hence, we model and subtract this early SCE component before fitting for the radioactive decay of ^{56}Ni. This methodology has been successfully used in the past (Yao et al. 2020) to model USSNe with extended envelopes.

We assume that for the early-time emission (t < 2 days; as seen in Figure 1) of SN2019wxt, the emission is dominated by the shock-cooling process. We used the Piro et al. (2021) shock-cooling model to constrain the SCE parameters such as mass ($M_{\rm ext}$), radius ($R_{\rm ext}$), and energy ($E_{\rm ext,\ 49}$) of the extended envelope. As mentioned previously, we fixed the time of the explosion for the model to $t_{\rm exp} \approx -4$ days based on the earliest upper limits available for SN2019wxt from our z-band observation. The SCE parameters were then assigned (wide) flat priors, as presented in Table 3. These priors were informed

Table 3
Parameters Used for the Early-time Shock-cooling Model and Their Priors

θ	Description	Prior
log$R_{\rm ext}$	$\log_{10}$ of radius of extended envelope (cm)	$\mathcal{U}$(1,18)
log$M_{\rm ext}$	$\log_{10}$ of mass of extended envelope ($M_\odot$)	$\mathcal{U}$(-4,-1)
$E_{\rm ext,49}$	Energy in extended envelope divided by 10^{49} erg	$\mathcal{U}$(0.1,20)

by low masses and large radii for extended envelopes inferred in previously known transients with early-time SCE. We perform the parameter inference using the emcee package MCMC implementation with a standard Gaussian log-likelihood function and with 100 walkers. The corner plot obtained from this analysis is displayed in Figure 13, which shows probability distributions for $\log_{10}M_{\rm ext}$, $\log_{10}R_{\rm ext}$, and $E_{\rm ext,49}$. We obtain the best-fitting model for parameter values of $M_{\rm ext} = 3.55^{+0.12}_{-0.11} \times 10^{-2}\ M_\odot$, $R_{\rm ext} = 5150.11^{+581.99}_{-513.27}\ R_\odot$, and $E_{\rm ext,49} = (10.00^{+6.82}_{-6.75}) \times 10^{49}$ erg.

We start the late-time emission ($t > 2$ days)-fitting procedure by subtracting the best-fit SCE model from the initial light curve to infer the radioactivity-powered properties of SN2019wxt. We use the ^{56}Ni decay model by Valenti et al. (2008) to constrain the nickel mass ($M_{\rm Ni}$), the characteristic photon diffusion timescale (τ_m), and the characteristic γ-ray timescale (t_0). The model parameters are assigned wide, flat priors, as presented in Table 4. We again perform the parameter inference using the emcee package MCMC implementation with a standard Gaussian log-likelihood function involving 100 walkers. The corner plot obtained from this MCMC is displayed in Figure 14. We obtain the best-fit radioactivity model for parameter values of $M_{\rm Ni} = 2.73^{+0.33}_{-0.18} \times 10^{-2} M_\odot$, $\tau_m = 4.35^{+1.16}_{-1.43}$ days, and $t_0 = 12.58^{+1.23}_{-1.34}$ days. The best-fit models for the shock-cooling emission and ^{56}Ni radioactive

Table 4
Parameters Used for the ^{56}Ni Decay Radioactivity Model and Their Priors

θ	Description	Prior
τ_m	Characteristic photon diffusion time (day)	$\mathcal{U}(2,6)$
log$M_{\rm Ni}$	$\log_{10}$ of nickel mass ($M_\odot$)	$\mathcal{U}(-4, -1.25)$
t_0	Characteristic γ-ray escape time (day)	$\mathcal{U}(8,100)$

decay along with total luminosity evolution are presented in Figure 9.

Based on our parameter estimations, we can calculate the ejecta mass using an update to the ^{56}Ni decay model (see Equation (1) in Lyman et al. 2016):

$$M_{\rm ej} = \left(\frac{\tau_m^2 \ \beta \ c \ v_{\rm ph}}{2 \ \kappa_{\rm opt}} \right), \quad (1)$$

where $\beta \simeq 13.8$ is a constant, $\kappa_{\rm opt} \approx 0.07$ cm^2 g^{-1} is the mean optical depth for a SESN, and $v_{\rm ph}$ is photospheric velocity.[21]

In order to approximately calculate the ejecta mass for SN2019wxt, we assumed that photospheric velocity ($v_{\rm ph}$) should be obtained close to the peak of the bolometric light curve. Therefore, to estimate this velocity, we use the evolution of blackbody radius ($R_{\rm bb}$) as an approximation for the change of the photospheric radius. We then assume a linear expansion of the radius around the second peak (from $t = 1$ day to $t =$ 15 days) to calculate the velocity of the ejecta. We find this ejecta velocity to be ≈9300 km s^{-1}.

Following from Equation (1) and estimated $v_{\rm ph}$, we find the ejecta mass to be $M_{\rm ej} \approx 0.20^{+0.12}_{-0.11} M_\odot$. This ejecta mass is of the same order of magnitude as the ejecta masses estimated for known USSNe objects SN2019dge (≈0.3$M_\odot$) and iPTF14gqr (≈0.2$M_\odot$), which highlights the USSNe nature of SN2019wxt. This ejecta mass and velocity translate to SN2019wxt's kinetic energy being $E_{\rm kin,ej} \approx (1.01^{+0.61}_{-0.55}) \times 10^{50}$ erg. We would like to note that due to the assumptions in modeling the emission from SN2019wxt coupled with the scarcity of early-time multiband observations, there may exist degeneracies between the model parameters, such as between the radius and the energy of the extended envelope (Piro 2015).

3.4. X-Ray Image Analysis

The primary analysis and calibration of X-ray data were performed with version 4.14 of Chandra's CIAO software package (Fruscione et al. 2006). The calibration of X-ray data used the database CALDBv4.9.7. We reprocessed the primary and secondary data using the automatic Chandra-*repro* script, resulting in new level 2 event and response files.

After this, we obtained X-ray images for the 0.3–8 keV energy range (Figure 10) and used *wavdetect* to extract all the sources in the region. However, no sources were found in the region of interest and spatially coincident with SN2019wxt. We used the Chandra *srcflx* routine to arrive at background count rates. This background rate allowed us to establish an upper limit on the source count rate. In this analysis we found the source to be undetectable at 6.51×10^{-6} cts s^{-1}. We used absorbed power with an index of 2.1 and assumed a neutral hydrogen density ($N_{\rm H}$) of 1.8×10^{20} cm^{-2} to convert this count rate into a 0.3–8 keV flux upper limit of $\lesssim 9.93 \times 10^{-17}$ erg cm^{-2} s^{-1}. Meanwhile, AGN of the host galaxy of SN2019wxt is detected with a 5σ confidence threshold with a count rate of 3.52×10^{-3} cts s^{-1}. Using an absorbed power law with an index of 1.7, this count rate corresponds to a flux of 5.87×10^{-14} erg cm^{-2} s^{-1}. The X-ray position for the galaxy coincides with the position reported in NED within the uncertainties.

[21] We substitute photospheric velocity ($v_{\rm ph}$) in the equation in lieu of the usual "scale velocity" given $v_{\rm ph}$ is observationally equivalent to the scale velocity at the maximum bolometric luminosity.

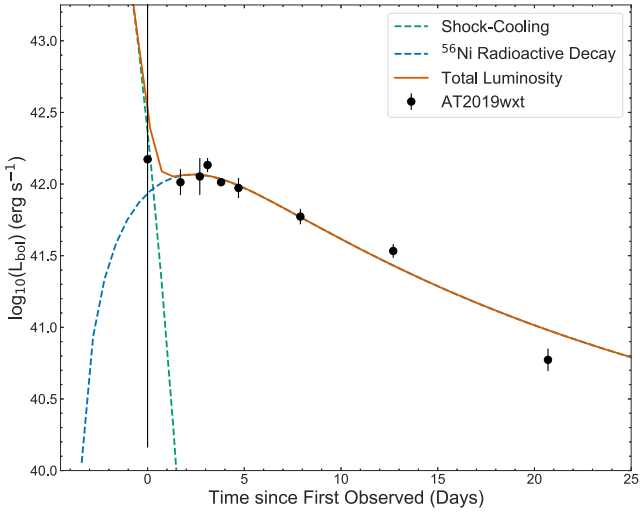

Figure 9. Bolometric light curve of SN2019wxt plotted with the best-fit shock-cooling model (dashed green line) and the best-fit ^{56}Ni decay radioactivity model (dashed blue line). The sum of the two models is shown with a solid red line.

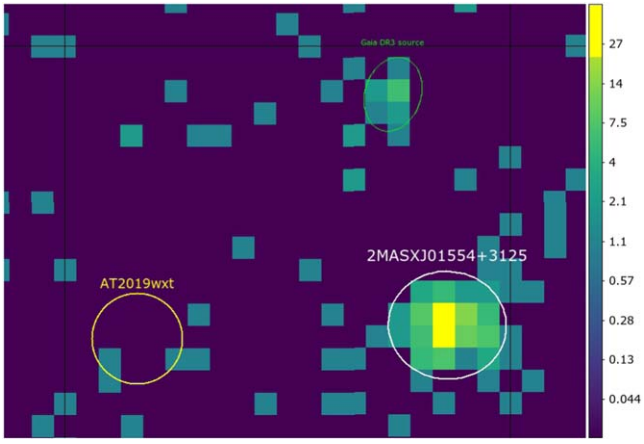

Figure 10. In this panel, we present a 0.3–10 keV Chandra image of SN2019wxt during the longest 100 ks observation. We plot a 1″ radius circle-centered optical position of SN2019wxt. The host-galaxy active galactic nucleus (AGN) is indicated by an ellipse of major and minor axes 1.″301 and 1.″189. We matched the coordinates of the host galaxy from Chandra and find a match in both the NED and Gaia catalogs. The image colors are presented in log scale and we do not observe any significant emission at the location of SN2019wxt, while the host galaxy is confidently detected at the 5σ level. We also see a faint Gaia transient in the field.

3.5. Radio Data Analysis

Since all observations in the *K* band (22 GHz) were upper limits, we proceed to discuss results from only the *X* (10 GHz) and *Ku* (15 GHz) bands. Figure 11 shows the radio flux density measurements at the location of SN2019wxt (top panel) and the host galaxy, KUG 0152+311 (bottom panel) in the VLA *X*

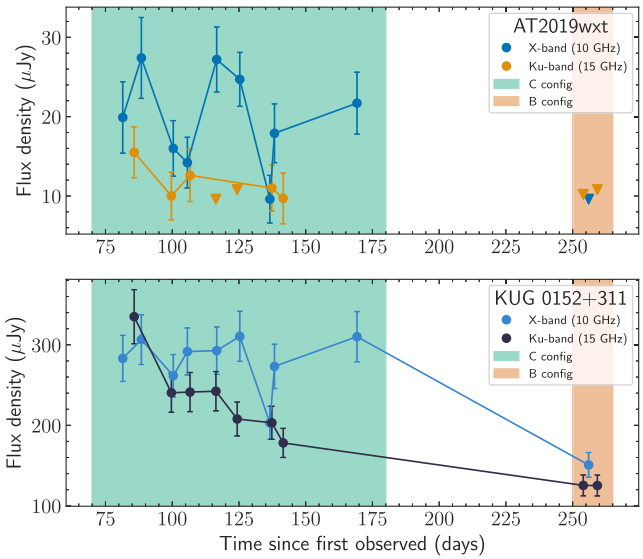

Figure 11. Plot of the radio flux density measurements at the location of SN2019wxt (top panel) in the *X* (10 GHz) and *Ku* (15 GHz) bands, compared to the peak flux density measurements of the host galaxy (bottom panel) as a function of time, as reported in Table 10. The downward pointing triangles are upper limits (see Section 2.4 for more details).

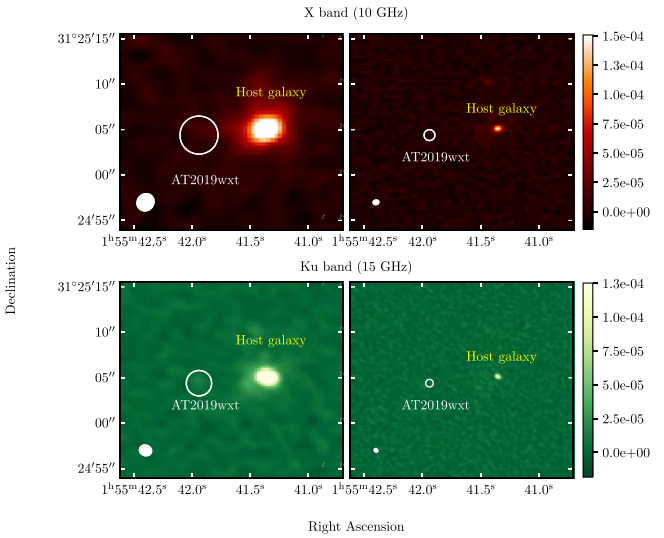

Figure 12. The host galaxy as seen in VLA configurations C (left) and B (right), in the *X* band (10 GHz; top) and *Ku* band (15 GHz; bottom). The white circles mark the position of SN2019wxt with a radius equal to the FWHM of the nominal VLA synthesized beam of each observation. The synthesized beam ellipse is shown on the left bottom of each panel and the color bars provide the flux density in units of Jy. See the text for discussion.

(10 GHz) and *Ku* (15 GHz) bands (see Table 10). The host galaxy (KUG 0152+311) is resolved in images taken in *X* (10 GHz) and *Ku* (15 GHz) bands with the VLA in its C configuration and is marginally resolved in both these bands for the B configuration observations. Moreover, as evident from Figure 12, the host-galaxy emission is likely contaminating our measurements at the location of SN2019wxt in observations taken with the VLA in its more compact C configuration. A strong host-galaxy contribution to the flux measured at the SN2019wxt location is also suggested by the fact that observations taken with the VLA in the more extended B configuration (see colored regions in Figure 11) show a drastic decrease in the measured flux density of the host galaxy, and return a nondetection at the location of SN2019wxt (see also Table 10). This is compatible with the hypothesis that the more tenuous extended emission from the host contaminates our C configuration measurements at the location of SN2019wxt, but goes undetected in the VLA B configuration (see also the right panels in Figure 12).

To test whether the flux we measure at the SN2019wxt location is dominated by host-galaxy emission, we computed the Pearson correlation coefficient to check for a potential correlation between such flux and host-galaxy flux density measurements (see, e.g., D'Ammando et al. 2019; Hillier et al. 2019). We find that the flux measured at the SN2019wxt location is strongly correlated with that measured for the host galaxy (99.32% in the *X* band and 98.71% in the *Ku* band). This correlation can be visualized by comparing the time variation of the flux measurements at the SN2019wxt location and that of the host galaxy (Figure 11). Next, to quantify the variability in the flux measurements obtained at the SN2019wxt location and for the SN2019wxt host galaxy, we use our *X*- and *Ku*-band data and adopt the statistical metrics described in Swinbank et al. (2015). We briefly introduce them here. We use N, F_ν, and σ_ν to represent the number of observations, flux density measurements, and the corresponding errors at frequency ν (see Table 10), respectively. The flux density

Table 5
Radio Variability Metrics for SN2019wxt Compared with SN1993J in *X* (10 GHz) and *Ku* (15 GHz) Bands Excluding Upper Limits

Freq. band	SN2019wxt		Host		SN1993J	
	V_ν	$P_{\rm var}$ (%)	V_ν	$P_{\rm var}$ (%)	V_ν	$P_{\rm var}$ (%)
X (10 GHz)	0.3	5.6	0.1	2.2	0.2	48.4
Ku (15 GHz)	0.2	3.3	0.2	32.6	0.2	4.2×10^{-3}

Note. See Section 3.5 for discussion.

coefficient of variation can be calculated as

$$V_\nu = \frac{1}{\overline{F_\nu}}\sqrt{\frac{N}{N-1}(\overline{F_\nu^2} - \overline{F_\nu}^2)}. \quad (2)$$

Assuming weights of $w_\nu = 1/\sigma_\nu^2$, the weighted average flux density is calculated as

$$\xi_{F_\nu} = \frac{\sum_{i=1}^{N} w_\nu F_{\nu,i}}{\sum_{i=1}^{N} w_\nu}. \quad (3)$$

Further, we calculate the reduced χ^2 using the above-defined weighted mean flux density:

$$\eta_\nu = \frac{1}{N-1}\sum_{i=1}^{N}\frac{(F_{\nu,i} - \xi_{F_\nu})^2}{\sigma_{\nu,i}^2}. \quad (4)$$

Using this metric we can calculate the probability for the source to be a variable as

$$P_{\rm var} = 1 - \int_{\eta_\nu'=\eta_\nu}^{\infty} p(\eta_\nu', N-1)\mathrm{d}\eta_\nu'. \quad (5)$$

where $p(x, n)$ is the χ^2 probability density function for x over n degrees of freedom.

Table 6
Parameters of Different Fast-evolving Transients—Redshift of the Host Galaxy, Host-galaxy Type, Peak Luminosity, and Decay Rate, with Respect to the Second Peak of g-band Observations, Ejecta Mass $M_{\rm ej}$, Nickel Mass $M_{\rm Ni}$, Radius, and Mass of Extended Envelope $R_{\rm ext}$, $M_{\rm ext}$

Transient Name	Redshift	Host Galaxy Type	Second Peak Magnitude	Decay Rate (g band) (mag day^{-1})	Ejecta Mass $M_{\rm ej}$ ($M_\odot$)	Nickel Mass $M_{\rm Ni}$ ($10^{-2}M_\odot$)	Envelope Radius $R_{\rm ext}$ (10^{13} cm)	Envelope Mass $M_{\rm ext}$ ($10^{-2}M_\odot$)
SN2019wxt	0.036	Compact	−16.6	0.41	$0.20^{+0.12}_{-0.11}$	$2.73^{+0.33}_{-0.18}$	$35.8^{+4.06}_{-3.68}$	$3.55^{+0.12}_{-0.11}$
SN2019dge	0.021	Compact	−15.5	0.13	$0.38^{+0.02}_{-0.02}$	$1.57^{+0.04}_{-0.03}$	$1.19^{+0.06}_{-0.05}$	$9.71^{+0.28}_{-0.27}$
iPTF14gqr	0.063	Spiral	−17.5	0.21	$0.24^{+0.02}_{-0.02}$	$8.14^{+0.14}_{-0.15}$	$6.09^{+8.73}_{-3.18}$	$2.59^{+0.46}_{-0.34}$
iPTF16hgs	0.017	Spiral	−15.1	0.17	$1.68^{+0.28}_{-0.25}$	$2.51^{+0.20}_{-0.22}$	$2.45^{+14.08}_{-1.80}$	$9.27^{+3.40}_{-2.48}$

Finally, we also compare the variability metrics computed for the flux measurements (excluding upper limits; see Table 10) at the location of SN2019wxt and the host galaxy, KUG 0152+311, with those that can be obtained from the radio light curves of the well-sampled, radio-loud Type IIb supernova SN1993J (Weiler et al. 2007) at the same timescales as our data. This comparison was made owing to the initial Type IIb classification of the event (as discussed in Section 2.2.2).

As evident from Table 5, SN2019wxt and its host galaxy display comparable variability statistics in the X band. The last is much smaller than the variability of SN1993J over the same timescales and in the same band. We also note that the same variability analysis for the X-band (10 GHz) observations of GW170817 yields a variability statistic of $P_{\rm var} = 55.7\%$ over timescales comparable to the ones of our radio observations of SN2019wxt. Thus, we exclude a GW170817-like radio counterpart for SN2019wxt.

The variability statistics in the Ku band (15 GHz) are more complex. A SN1993J-like transient would have varied very little in this band over the observed timescales. Hence, the lack of substantial variability in this band would not necessarily indicate a host-galaxy origin for the emission measured at the SN2019wxt location. Moreover, we note that in the Ku band the flux from the core of the host varies substantially and more than the flux measured at the position of SN2019wxt.

Overall, our results suggest that the radio detections at the location of SN2019wxt are likely to be related to host-galaxy contamination. There is little evidence for the type of variability that would be expected for SN1993J-like or GW170817-like events.

4. Discussion and Conclusions

In this paper, we present optical, NIR, radio, and X-ray observations and analyses for the peculiar and rapidly evolving transient SN2019wxt. The source SN2019wxt was found on 2019 December 16 UTC 07:19:12 during the search for an electromagnetic counterpart to the GW trigger S191213g. At the time it was the prime optical counterpart of interest given its rapidly evolving light curve akin to kilonova expected from a BNS merger. The source was intensely followed with *grizyJ* bands' photometric and spectroscopic observations for approximately 20.7 days post the initial discovery. The optical light curve shows a prominent double-peaked structure in the i band and a less prominent structure in the g band. The second peak has an absolute magnitude $g \sim i \sim -16.6$ mag. The bolometric light curve derived from the multiband photometry displayed at least one peak, though with relatively large uncertainties. These uncertainties are a result of a lack of multiband observations of SN2019wxt in the early-time observations ($t \lesssim 2$ days). We characterize the optical/NIR light curve of SN2019wxt using a combination of an early-time shock-cooling component and a late-time ^{56}Ni decay component. We estimate that the SCE arises from an extended envelope of mass $\approx 0.035\,M_\odot$ and radius $\approx 35.8 \times 10^{13}$ cm. We also estimate that the radioactivity-powered component is composed of nickel mass $\approx 0.027 M_\odot$ from which we estimate the ejecta mass $\approx 0.20 M_\odot$.

Our long-term radio and X-ray observations of SN2019wxt spanned a period starting from 3.7 days after the initial GW trigger discovery and up to 320 days. Our X-ray observations show no evidence of excess emission at the location of SN2019wxt. Previously, USSNe have been targeted with Swift-XRT observations (De et al. 2018b; Yao et al. 2020); however, no X-ray emission was observed for these USSNe with multiepochal X-ray observations at a flux threshold of $\lesssim 10^{-14}$ erg cm^{-2} s^{-1}. In this work, with long-term Chandra high-resolution X-ray observations of the source, we obtain one of the most stringent nondetection limits at $\lesssim 10^{-17}$ erg cm^{-2} s^{-1}.

On the other hand, while our radio observations show excess emission at the location of SN2019wxt, there is little evidence for SN1993j-like or GW170817-like variability over the timescales of our follow-up. We also discussed the possibility of host-galaxy contamination at the location of SN2019wxt in the radio frequencies (especially at the lowest radio frequencies).

4.1. Transient Progenitor and Nature of the System

The double-peaked light curve in the i band indicated the presence of an extended envelope around the progenitor of SN2019wxt. This envelope likely originated from the extreme stripping of the outer layers of this progenitor star (Nakar & Piro 2014). We find that the radius of the extended envelope inferred from our parameter estimation is 1 order of magnitude larger than those of previously known USSNe candidates (see Table 6). We would like to note that the uncertainties for the radius of the extended envelope are underestimated due to the lack of early-time observations, for which the shock-cooling model was fitted. For rapidly evolving transients such as USSNe, it is extremely critical to obtain observations in more than one band (specifically, the redder bands) to get a better constraint on the luminosity and rise time of the first peak. These early-time constraints can help provide a better estimate for the mass and radius of envelopes surrounding progenitors of USSNe. In addition to early-time multiband observations, early-time spectroscopic observations during the first peak can help break the degeneracy between the radius of the envelope and the energy of the USSN by providing measurements of the velocity and composition of the extended material (Piro 2015). However, in this work, we only have spectroscopic observations taken prior to the first peak, as indicated in Figure 1. For

Table 7
Summary of Optical Observations of SN2019wxt

Obs. Time (MJD)	Filter	Magnitude (mag)	Mag Error (mag)
Pan-STARRS (McBrien et al. 2019a)			
58829.348	*z*	>21.0	...
58830.379	*z*	>20.3	...
58832.305	*i*	>19.4	...
58833.305	*i*	19.29	0.05
58833.320	*i*	19.23	0.07
58833.335	*i*	19.28	0.07
Palomar P60 inch (Fremling 2019)			
58836.687	*g*	19.43	0.10
58836.703	*g*	19.42	0.11
58836.684	*r*	19.28	0.11
58836.700	*r*	19.27	0.18
58836.690	*i*	19.28	0.13
58836.706	*i*	19.30	0.12
Lulin 1 m (Kong 2019)			
58836.446	*g*	19.32	0.04
58836.446	*r*	19.27	0.03
58836.446	*i*	19.38	0.06
DCT (Dichiara & a larger Collaboration 2019)			
58837.126	*g*	19.67	0.02
58837.114	*r*	19.30	0.02
58837.120	*i*	19.52	0.01
58837.126	*z*	19.51	0.03
Pan-STARRS (Huber et al. 2019)			
58836.434	*g*	19.23	0.09
58841.211	*g*	20.25	0.07
58836.436	*r*	19.19	0.07
58841.213	*r*	20.03	0.05
58836.438	*i*	19.21	0.07
58841.214	*i*	19.88	0.04
58836.439	*z*	19.34	0.11
58841.216	*z*	19.75	0.05
58836.441	*y*	19.31	0.22
58841.218	*y*	19.68	0.12
Wendelstein 2 m (Hopp et al. 2020)			
58835.000	*g*	19.59	0.08
58836.000	*g*	19.64	0.11
58838.000	*g*	19.91	0.06
58846.000	*g*	22.58	0.05
58854.000	*g*	23.49	0.08
58835.000	*i*	20.00	0.09
58836.000	*i*	19.74	0.09
58838.000	*i*	19.73	0.06
58846.000	*i*	20.82	0.06
58854.000	*i*	22.54	0.07
58835.000	*J*	20.22	0.08
58836.000	*J*	19.14	0.11
58838.000	*J*	18.92	0.10
58846.000	*J*	19.71	0.11
58854.000	*J*	20.65	0.12

Note. The observation of SN2019wxt at MJD 58833.305 sets the reference epoch for this work.

the spectra obtained prior to the peak by Vogl et al. (2019), the velocity of the absorption lines is reported to be between 7000 and 10,000 km s^{-1}, which is consistent with the ejecta velocity we estimate using the photospheric radius evolution.

An estimation of the ejecta mass can provide insight into the process likely causing the stripping of the outer layers of the progenitor. One of the mechanisms that can strip the envelope to this extent is binary mass transfer. Predictions from different stellar evolution models link the ejecta mass to the nature of the progenitor system. Single-star evolutionary models of massive stars predict relatively high ejecta masses ($M_{ej} > 3M_{\odot}$; Meynet & Maeder 2005; Eldridge & Vink 2006; Georgy et al. 2009), much larger than that found for SN2019wxt ($M_{ej} \approx 0.20M_{\odot}$). On the contrary, binary stellar evolution models predict that most Type Ib/c SNe emerged from massive stars in close binary systems, with ejecta masses ranging from 1 to $5M_{\odot}$ (Dessart et al. 2012; Eldridge et al. 2013). An even greater degree of stripping can occur in a binary system, further reducing ejecta masses to the order of $0.1M_{\odot}$ and ^{56}Ni mass of the order of 0.01 $M_{\odot}$—as observed in USSNe (Tauris et al. 2013). These USSNe explosions are hence posited to be progenitors of double NS systems. The ejecta mass estimated for SN2019wxt is of the same order of magnitude as that of previously known USSNe candidates. Based on our photometric and spectroscopic analysis, we identify SN2019wxt as a strong USSNe candidate. Antier et al. (2020), in their work conducting EM follow-up of O3 events, also concluded that the rapidly declining nature of the peculiar transient SN2019wxt could likely be due to the interaction of ejecta with circumstellar material. They also suggest that the supernova could be a result of binary evolution. While this paper was under development, the ENGRAVE collaboration (Agudo et al. 2022) independently analyzed SN2019wxt and arrived at a similar conclusion for source characterization.

Spectroscopic observations can provide a clue with respect to the extent of stripping that the progenitor underwent. However, given only two USSNe are currently known, we do not yet have a spectral model for these sources with characteristic features. However, some of the spectral lines that we list in Table 2 have been previously observed in both SN2019dge and iPTF14gqr sources. In our spectroscopic analysis, we see no broad hydrogen lines, indicating a loss of hydrogen envelope in the system (Filippenko 1997).

SN2019wxt was located in a compact host galaxy, KUG 0152+311, at an offset of 0.″5 S, 7.″7 E from the galactic center. The USSNe candidate SN2019dge was also located in a compact host galaxy SDSS J173646.73+503252.3 at a projected offset of 0.″5 from the center. Meanwhile, the USSNe candidate iPTF14gqr was located in the outskirts of a tidally interacting spiral galaxy IV Zw 155 at a projected offset of 24″ from the center. The location of SN2019wxt at a relatively closer distance to the host galaxy's center matches with the prediction of Tauris et al. (2015) that USSNe are found to occur close to their host galaxy's star-forming regions.

4.2. SN2019wxt and Searching for USSNe

Systematic all-sky surveys such as Zwicky Transient Facility (Bellm et al. 2019; Graham et al. 2019) and intermediate Palomar Transient Factory (iPTF; Law et al. 2009) have accelerated searches for rapidly evolving transients (e.g., Ho et al. 2020; Andreoni et al. 2021). We can visualize the progress in transients searches in the last decade based on two key parameters: (i) the characteristic timescale of the transients, defined as the time taken for the magnitude to change by 0.75 mag from the peak, and (ii) peak luminosity. A classification plot based on these quantities called the phase-

space diagram (see Figure 1; Nugent et al. 2015) helps visualize the spread between different transients, such as SN, USSNe, stripped-envelope SN, kilonovae, etc. In this plot, we observe that the transient SN2019wxt lies in the relatively slower-evolving and greater-luminosity regime compared to the kilonova AT2017gfo. However, post the second peak it evolves faster compared to the USSNe candidates (SN2019dge and iPTF14gqr) and the Ca-rich gap transient (iPTF16hgs). It also shows blackbody parameters intermediate to kilonovae and USSNe, as seen in Figure 7. We expect upcoming wide-field surveys to open up a new discovery space for faster, fainter transients at large redshifts. A larger sample of transients populating the phase-space diagram will be able to outline classes and subclasses of transients, such as SESNe (see Figure 18 in Moriya et al. 2017), and provide an understanding of possible central energy sources for these USSNe (Sawada et al. 2022).

The presence of an early-time peak in SN2019wxt is dominated by SCE. This SCE links to the progenitor stripping and highlights the importance of observing such rapidly evolving transients in the early stages. One of the main reasons this early-time peak was captured for SN2019wxt is that the source was coincidentally situated within the LIGO BNS merger region. Hence, global multiband optical observation campaigns were launched to search for a rapidly evolving counterpart to the GW trigger S191213g (Kasliwal et al. 2020). Andreoni et al. (2019) highlight the potential of the high-cadence observational campaign of the Vera C. Rubin Observatory's Legacy Survey of Space and Time (LSST; Ivezić et al. 2019) in capturing an early SCE emission peak in SNe, which can provide important constraints on the progenitor star. Currently, only two USSNe candidates beyond SN2019wxt are known among nearly 10,000 SNe found thus far. LSST is expected to improve SNe statistics up to a million SNe/yr (LSST Science Collaboration et al. 2009). Scaling to the first order from the current ratio of USSNe to the SNe population, we expect $\sim$20 USSNe yr^{-1} with LSST at larger redshifts. Early-time peak capture of these USSNe will be important in arriving at properties of the source class as highlighted by SN2019wxt.

Acknowledgments

J.M.D. and H.S. acknowledge support from the Amsterdam Academic Alliance (AAA) Program, and the European Research Council (ERC) European Union's Horizon 2020 research and innovation program (grant agreement No. 679633; Exo-Atmos). This work is part of the research program VIDI New Frontiers in Exoplanetary Climatology, with project number 614.001.601, which is (partly) financed by the Dutch Research Council (NWO). F.H. and A.J. would like to thank observational support from Chandra X-ray observatory staff. Their work was supported by Chandra observational grant award GO0-21067X. A.B. and A.C. acknowledge support from the National Science Foundation via grant No. 1907975. The National Radio Astronomy Observatory is a facility of the National Science Foundation operated under a cooperative agreement by Associated Universities, Inc. H.S. would like to thank Yuhan Yao for the methodologies developed to characterize USSNe that we have used in this work and for the insightful discussions throughout the course of this work. Nayana A.J. would like to acknowledge DST-INSPIRE Faculty Fellowship (IFA20- PH-259) for supporting this research.

Appendix A
Observation Tables

In this section, we present tables summarizing optical photometric (Table 7), optical spectroscopic (Table 8), X-ray (Table 9), and radio (Table 10) observations of SN2019wxt. These observations were obtained from +3 days to +323 days from the initial GW trigger.

Table 8
Summary of Optical Spectroscopic Observations of SN2019wxt

Obs. Start (MJD)	Telescope	Instrument	Wavelength (Å)	Exposure Time (s)	Resolution
58835.753	HCT-IIA	HFOSC2	3800–7500	3600	1200
58836.035	NTT-EPESSTO	EFOSC/1.57	3985–9315	1200.0061	18 Å
58836.059	ESO-VLT-U1	CCDF-FORS2	3400–9600	1499.9388	10 Å
58836.216	LBT	MODS2	3200–9750	3600	4 Å

Table 9
Summary of Chandra X-Ray Imaging Observations of SN2019wxt, Over a Period of 233 Days

Obs. ID	Obs. Start Time (MJD)	Effective Exposure (ks)
22458	58920.64792	49.41
23193	58922.27917	46.45
22459	59017.46736	42.51
23283	59018.33472	49.24
22460	59077.09375	33.45
22461	59152.85	19.82
24848	59153.8	14.89

Note. All observations were obtained with an ACIS-S3 chip in TE mode and VFAINT telemetry format.

Table 10
VLA Observations of SN2019wxt Along with the Integrated Flux Measurements of the Host Galaxy KUG 0152+311

Obs. Time (MJD)	Time Elapsed (days)	VLA config.	VLA band	Obs. Freq. (GHz)	Source Flux (μJy) $F_\nu \pm \sigma_\nu$	Galaxy Flux (μJy) peak $F_\nu \pm \sigma_\nu$
58837.0	3.7	D	*K*	22.0	<25.1	452 ± 91
58914.8	81.5	C	*X*	10.0	19.9 ± 4.5	283 ± 29
58919.1	85.7	C	*Ku*	15.4	15.5 ± 3.2	335 ± 34
58921.7	88.4	C	*X*	9.3	27.4 ± 5.1	306 ± 31
58933.0	99.7	C	*Ku*	15.4	10.0 ± 3.0	240 ± 24
58933.7	100.4	C	*X*	9.8	16.0 ± 3.5	262 ± 26
58939.0	105.7	C	*X*	10.0	14.2 ± 3.2	292 ± 29
58940.0	106.7	C	*Ku*	15.4	12.6 ± 3.3	241 ± 24
58943.7	110.4	C	*K*	22.0	<21.6	152 ± 31
58949.7	116.4	C	*Ku*	15.4	<9.6	242 ± 24
58950.0	116.7	C	*X*	9.7	27.2 ± 4.1	293 ± 29
58956.7	123.3	C	*K*	22.0	<11.7	233 ± 47
58957.6	124.3	C	*Ku*	15.3	<10.8	208 ± 21
58958.6	125.3	C	*X*	10.0	24.7 ± 3.4	311 ± 31
58969.9	136.6	C	*X*	10.0	9.6 ± 3.0	203 ± 20
58970.6	137.3	C	*Ku*	14.8	11.0 ± 2.9	203 ± 20
58971.6	138.3	C	*X*	9.3	17.9 ± 3.7	273 ± 28
58974.9	141.6	C	*Ku*	15.7	9.7 ± 3.2	178 ± 18
59002.5	169.2	C	*X*	9.4	21.7 ± 3.9	310 ± 31
59087.3	254.0	B	*Ku*	15.0	<10.2	125 ± 13
59089.3	256.0	B	*X*	10.0	<9.6	151 ± 15
59092.6	259.3	B	*Ku*	15.0	<10.8	125 ± 13

Note. All epochs are with respect to the first optical detection (MJD 58833.305). See Section 2.4 for more details.

Appendix B
Parameter Estimation

In this section, we present corner plots for our MCMC analysis using the shock-cooling model (Figure 13) and the radioacitvity model (Figure 14).

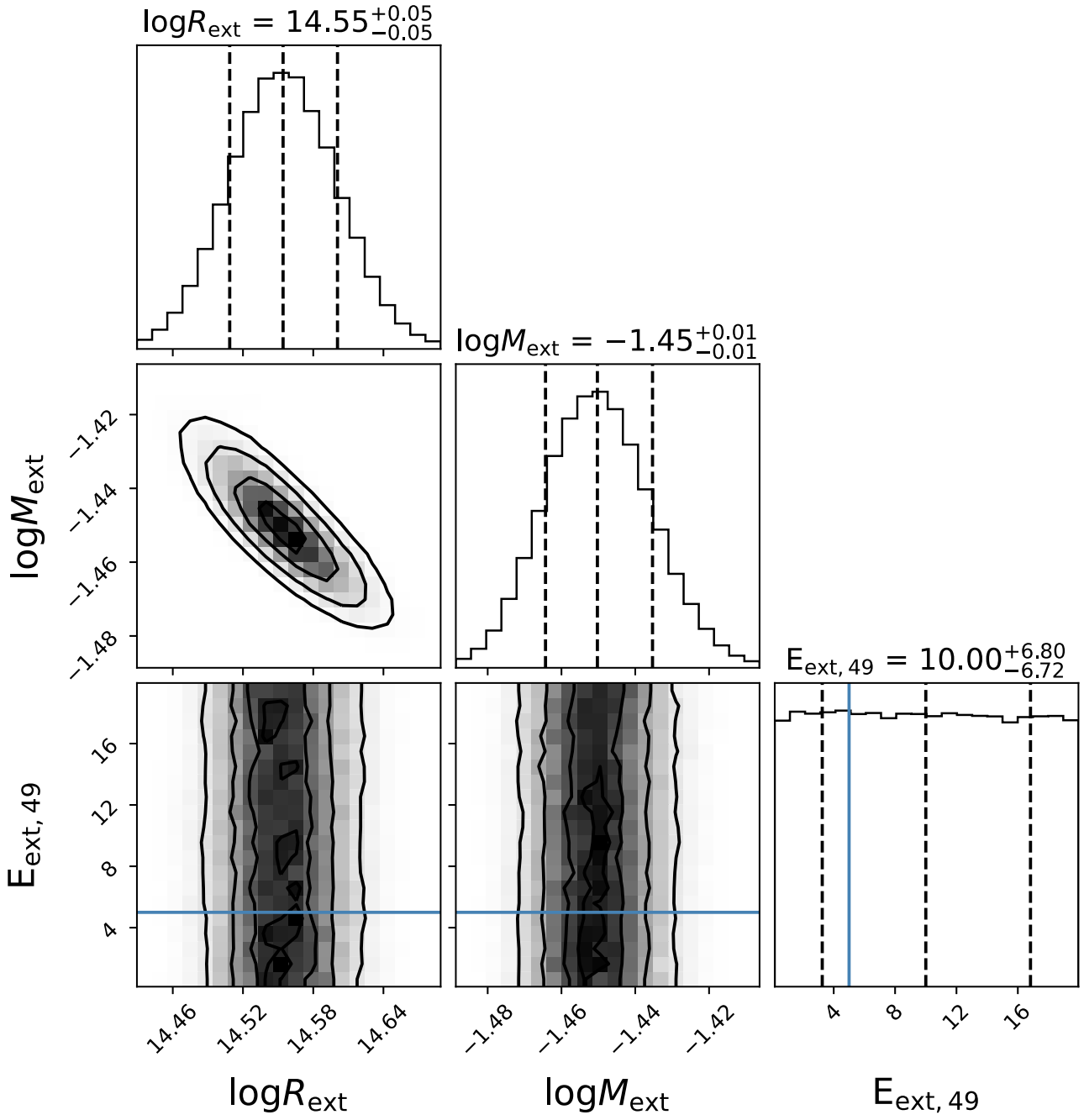

Figure 13. Corner plot obtained from the shock-cooling model displaying the constraints on the posteriors of $\log_{10}$ of mass of the envelope ($\log M_{\rm env}$), $\log_{10}$ of radius of the envelope ($\log R_{\rm env}$), and energy of the envelope ($E_{\rm ext,49}$). Along the diagonal, the vertical dashed lines on the histogram indicate the estimate of the best-fit (median) value and the 68% confidence intervals. The contours represent the 16$^{\rm th}$, 50$^{\rm th}$, and 84$^{\rm th}$ percentile for the respective phase space.

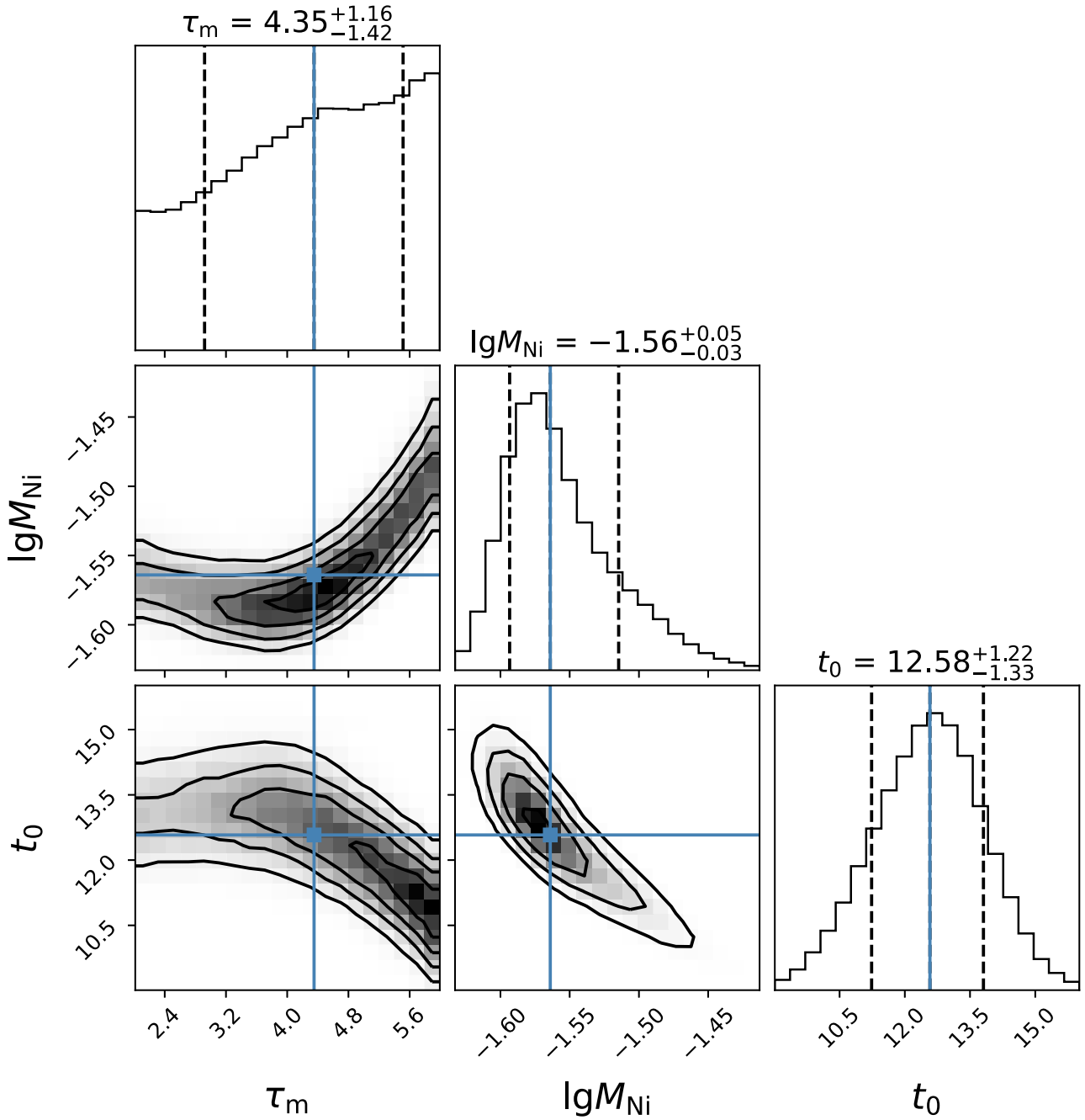

Figure 14. Corner plot obtained from the radioactivity model displaying the constraints on the posteriors of t_0, $\log_{10} M_{Ni}$, and τ_m derived from the radioactivity model. Along the diagonal, the vertical dashed lines on the histogram indicate the estimate of the best-fit (median) value and the 68% confidence intervals. The contours represent the 16th, 50th, and 84th percentile for the respective phase space.

ORCID iDs

Hinna Shivkumar https://orcid.org/0000-0001-9289-0570
Amruta D. Jaodand https://orcid.org/0000-0002-3850-6651
Arvind Balasubramanian https://orcid.org/0000-0003-0477-7645
Christoffer Fremling https://orcid.org/0000-0002-4223-103X
Alessandra Corsi https://orcid.org/0000-0001-8104-3536
Anastasios Tzanidakis https://orcid.org/0000-0003-0484-3331
Samaya Nissanke https://orcid.org/0000-0001-6573-7773
Mansi Kasliwal https://orcid.org/0000-0002-5619-4938
Murray Brightman https://orcid.org/0000-0002-8147-2602
Geert Raaijmakers https://orcid.org/0000-0002-9397-786X
Kristin Kruse Madsen https://orcid.org/0000-0003-1252-4891
Dario Carbone https://orcid.org/0000-0002-6575-4642
Nayana A. J. https://orcid.org/0000-0002-8070-5400
Jean-Michel Désert https://orcid.org/0000-0002-0875-8401
Igor Andreoni https://orcid.org/0000-0002-8977-1498

References

Abbott, B. P., Abbott, R., Abbott, T. D., et al. 2017, PhRvL, 119, 161101
Agudo, I, Amati, L., Bauer, F. E., et al. 2022, arXiv:2208.09000
Andreoni, I., Ackley, K., Cooke, J., et al. 2017, PASA, 34, e069
Andreoni, I., Anand, S., Bianco, F. B., et al. 2019, PASP, 131, 068004
Andreoni, I., Coughlin, M. W., Kool, E. C., et al. 2021, ApJ, 918, 63
Antier, S., Agayeva, S., Almualla, M., et al. 2020, MNRAS, 497, 5518
Arcavi, I., Hosseinzadeh, G., Howell, D. A., et al. 2017a, Natur, 551, 64
Arcavi, I., McCully, C., Hosseinzadeh, G., et al. 2017b, ApJL, 848, L33
Becerra-Gonzalez, J. & a larger Collaboration 2019, GCN, 26521, 1
Begelman, M. C., & Sarazin, C. L. 1986, ApJL, 302, L59
Bellm, E. C., Kulkarni, S. R., Graham, M. J., et al. 2019, PASP, 131, 018002
Bida, T. A., Dunham, E. W., Massey, P., & Roe, H. G. 2014, Proc. SPIE, 9147, 91472N
Blagorodnova, N., Neill, J. D., Walters, R., et al. 2018, PASP, 130, 035003
Cenko, S. B., Fox, D. B., Moon, D.-S., et al. 2006, PASP, 118, 1396
Clocchiatti, A., Wheeler, J. C., Benetti, S., & Frueh, M. 1996, ApJ, 459, 547
Coulter, D. A., Foley, R. J., Kilpatrick, C. D., et al. 2017, Sci, 358, 1556
Cowperthwaite, P. S., Berger, E., Villar, V. A., et al. 2017, ApJL, 848, L17
D'Ammando, F., Raiteri, C. M., Villata, M., et al. 2019, MNRAS, 490, 5300
De, K., Kasliwal, M. M., Cantwell, T., et al. 2018a, ApJ, 866, 72
De, K., Kasliwal, M. M., Ofek, E. O., et al. 2018b, Sci, 362, 201
Dessart, L., Hillier, D. J., Li, C., & Woosley, S. 2012, MNRAS, 424, 2139
Dichiara, S. & a larger Collaboration 2019, GCN, 26517, 1
Drout, M. R., Piro, A. L., Shappee, B. J., et al. 2017, Sci, 358, 1570
Drout, M. R., Soderberg, A. M., Mazzali, P. A., et al. 2013, ApJ, 774, 58
Dutta, A., Kumar, B., Kumar, H., et al. 2019, GCN, 26490, 1
Eldridge, J. J., Fraser, M., Smartt, S. J., Maund, J. R., & Crockett, R. M. 2013, MNRAS, 436, 774
Eldridge, J. J., & Vink, J. S. 2006, A&A, 452, 295
Evans, P. A., Cenko, S. B., Kennea, J. A., et al. 2017, Sci, 358, 1565
Filippenko, A. V. 1997, ARA&A, 35, 309
Fitzpatrick, E. L. 1999, PASP, 111, 63
Foley, R. J., Chornock, R., Filippenko, A. V., et al. 2009, AJ, 138, 376
Foreman-Mackey, D., Hogg, D. W., Lang, D., & Goodman, J. 2013, PASP, 125, 306
Fremling, C. 2019, GCN, 26500, 1
Fremling, C., Sollerman, J., Taddia, F., et al. 2016, A&A, 593, A68
Fruscione, A., McDowell, J. C., Allen, G. E., et al. 2006, Proc. SPIE, 6270, 62701V
Gaia Collaboration 2020, yCat, I/350
Gal-Yam, A., Arcavi, I., Ofek, E. O., et al. 2014, Natur, 509, 471
Georgy, C., Meynet, G., Walder, R., Folini, D., & Maeder, A. 2009, A&A, 502, 611
Goodman, J., & Weare, J. 2010, CAMCS, 5, 65
Graham, M. J., Kulkarni, S. R., Bellm, E. C., et al. 2019, PASP, 131, 078001
Haggard, D., Nynka, M., Ruan, J. J., et al. 2017, ApJL, 848, L25
Hajela, A., Margutti, R., Bright, J. S., et al. 2022, ApJL, 927, L17
Hillier, T., Brown, M. L., Harrison, I., & Whittaker, L. 2019, MNRAS, 488, 5420
Ho, A. Y. Q., Perley, D. A., Kulkarni, S. R., et al. 2020, ApJ, 895, 49
Hopp, U., Kluge, M., Goessl, C., Ries, C., & Schmidt, M. 2020, GCN, 27057, 1
Huber, M. E., Smartt, S. J., McBrien, O., & Schultz, K. C. C. A. S. B. 2019, GCN, 26577, 1
Izzo, L., Malesani, D. B., Heintz, K. E., et al. 2019, GCN, 26491, 1
Jacobson-Galán, W. V., Margutti, R., Kilpatrick, C. D., et al. 2020, ApJ, 898, 166
Ivezić, Ž., Kahn, S. M., Tyson, J. A., et al. 2019, ApJ, 873, 111
Kasliwal, M. M., Anand, S., Ahumada, T., et al. 2020, ApJ, 905, 145
Kasliwal, M. M., Kulkarni, S. R., Gal-Yam, A., et al. 2010, ApJL, 723, L98
Kasliwal, M. M., Nakar, E., Singer, L. P., et al. 2017, Sci, 358, 1559
Kong, A. 2019, GCN, 26503, 1
Kumar, B., Pandey, S. B., Sahu, D. K., et al. 2013, MNRAS, 431, 308
Lang-Bardl, F., Bender, R., Goessl, C., et al. 2016, Proc. SPIE, 9908, 990844
Law, N. M., Kulkarni, S. R., Dekany, R. G., et al. 2009, PASP, 121, 1395
LIGO Scientific Collaboration, Virgo Collaboration 2019a, GCN, 26402, 1
LIGO Scientific Collaboration, Virgo Collaboration 2019b, GCN, 26417, 1
Lipunov, V. M., Gorbovskoy, E., Kornilov, V. G., et al. 2017, ApJL, 850, L1
LSST Science Collaboration, Abell, P. A., Allison, J., et al. 2009, arXiv:0912.0201
Lyman, J. D., Bersier, D., James, P. A., et al. 2016, MNRAS, 457, 328
McBrien, O., Smartt, S. J., Smith, K. W., et al. 2019a, GCN, 26485, 1
McBrien, O. R., Smartt, S. J., Chen, T.-W., et al. 2019b, ApJL, 885, L23
McLaughlin, S., Smartt, S. J., Smith, K. W., et al. 2019, TNSAN, 154, 1
McMullin, J. P., Waters, B., Schiebel, D., Young, W., & Golap, K. 2007, in ASP Conf. Ser. 376, Astronomical Data Analysis Software and Systems XVI, ed. R. A. Shaw, F. Hill, & D. J. Bell (San Francisco, CA: ASP), 127
Meynet, G., & Maeder, A. 2005, A&A, 429, 581
Moriya, T. J., Mazzali, P. A., Tominaga, N., et al. 2017, MNRAS, 466, 2085
Müller Bravo, T., Chen, T. W., Fraser, M., et al. 2019, GCN, 26494, 1
Nakar, E., & Piro, A. L. 2014, ApJ, 788, 193
Nicholl, M., Berger, E., Kasen, D., et al. 2017, ApJL, 848, L18
Nugent, P., Cao, Y., & Kasliwal, M. 2015, Proc. SPIE, 9397, 1
Pian, E., D'Avanzo, P., Benetti, S., et al. 2017, Natur, 551, 67
Piro, A. L. 2015, ApJL, 808, L51
Piro, A. L., Haynie, A., & Yao, Y. 2021, ApJ, 909, 209
Pod 2001, in ASP Conf. Ser. 229, Evolution of Binary and Multiple Star Systems; A Meeting in Celebration of Peter Eggleton's 60th Birthday (San Francisco, CA: ASP)
Podsiadlowski, P., Joss, P. C., & Hsu, J. J. L. 1992, ApJ, 391, 246
Sawada, R., Kashiyama, K., & Suwa, Y. 2022, ApJ, 927, 223
Smartt, S. J., Chen, T. W., Jerkstrand, A., et al. 2017, Natur, 551, 75
Smith, N., Li, W., Filippenko, A. V., & Chornock, R. 2011, MNRAS, 412, 1522
Srivastav, S., & Smartt, S. J. 2019, GCN, 26493, 1
Stritzinger, M. D., Hsiao, E., Valenti, S., et al. 2014, A&A, 561, A146
Swinbank, J. D., Staley, T. D., Molenaar, G. J., et al. 2015, A&C, 11, 25
Tanvir, N. R., Levan, A. J., González-Fernández, C., et al. 2017, ApJL, 848, L27
Tauris, T. M., Kramer, M., Freire, P. C. C., et al. 2017, ApJ, 846, 170
Tauris, T. M., Langer, N., Moriya, T. J., et al. 2013, ApJL, 778, L23
Tauris, T. M., Langer, N., & Podsiadlowski, P. 2015, MNRAS, 451, 2123
The LIGO Scientific Collaboration, the Virgo Collaboration, the KAGRA Collaboration, et al. 2021, arXiv:2111.03606
Troja, E., Piro, L., van Eerten, H., et al. 2017, Natur, 551, 71
Utsumi, Y., Tanaka, M., Tominaga, N., et al. 2017, PASJ, 69, 101
Valeev, A. F., Castro-Rodriguez, N. & a larger Collaboration 2019, GCN, 26591, 1
Valenti, S., Benetti, S., Cappellaro, E., et al. 2008, MNRAS, 383, 1485
Valenti, S., Pastorello, A., Cappellaro, E., et al. 2009, Natur, 459, 674
Valenti, S., Sand, D. J., Yang, S., et al. 2017, ApJL, 848, L24
Vallely, P. 2019, GCN, 26508, 1
Vogl, C., Floers, A., Taubenberger, S., Hillebrandt, W., & Suyu, S. 2019, GCN, 26504, 1
Weiler, K. W., Williams, C. L., Panagia, N., et al. 2007, ApJ, 671, 1959
Woosley, S. E., & Weaver, T. A. 1995, ApJS, 101, 181
Yao, Y., De, K., Kasliwal, M. M., et al. 2020, ApJ, 900, 46
Yoon, S.-C. 2017, MNRAS, 470, 3970
Yoon, S. C., Woosley, S. E., & Langer, N. 2010, ApJ, 725, 940